NASA/TM—2018-219988

Modeling-Driven Damage Tolerant Design of Graphene Nanoplatelet/Carbon Fiber/Epoxy Hybrid Composite Panels for Full-Scale Aerospace Structures

Julie M. Tomasi, William A. Pisani, Sorayot Chinkanjanarot, and Aaron S. Krieg
Michigan Technological University, Houghton, Michigan

Evan J. Pineda, Brett A. Bednarcyk, and Sandi G. Miller
Glenn Research Center, Cleveland, Ohio

Julia A. King, Ibrahim Miskioglu, and Gregory M. Odegard
Michigan Technological University, Houghton, Michigan

September 2018

NASA STI Program . . . in Profile

Since its founding, NASA has been dedicated to the advancement of aeronautics and space science. The NASA Scientific and Technical Information (STI) Program plays a key part in helping NASA maintain this important role.

The NASA STI Program operates under the auspices of the Agency Chief Information Officer. It collects, organizes, provides for archiving, and disseminates NASA's STI. The NASA STI Program provides access to the NASA Technical Report Server—Registered (NTRS Reg) and NASA Technical Report Server—Public (NTRS) thus providing one of the largest collections of aeronautical and space science STI in the world. Results are published in both non-NASA channels and by NASA in the NASA STI Report Series, which includes the following report types:

- TECHNICAL PUBLICATION. Reports of completed research or a major significant phase of research that present the results of NASA programs and include extensive data or theoretical analysis. Includes compilations of significant scientific and technical data and information deemed to be of continuing reference value. NASA counter-part of peer-reviewed formal professional papers, but has less stringent limitations on manuscript length and extent of graphic presentations.

- TECHNICAL MEMORANDUM. Scientific and technical findings that are preliminary or of specialized interest, e.g., "quick-release" reports, working papers, and bibliographies that contain minimal annotation. Does not contain extensive analysis.

- CONTRACTOR REPORT. Scientific and technical findings by NASA-sponsored contractors and grantees.

- CONFERENCE PUBLICATION. Collected papers from scientific and technical conferences, symposia, seminars, or other meetings sponsored or co-sponsored by NASA.

- SPECIAL PUBLICATION. Scientific, technical, or historical information from NASA programs, projects, and missions, often concerned with subjects having substantial public interest.

- TECHNICAL TRANSLATION. English-language translations of foreign scientific and technical material pertinent to NASA's mission.

For more information about the NASA STI program, see the following:

- Access the NASA STI program home page at http://www.sti.nasa.gov

- E-mail your question to help@sti.nasa.gov

- Fax your question to the NASA STI Information Desk at 757-864-6500

- Telephone the NASA STI Information Desk at 757-864-9658

- Write to:
  NASA STI Program
  Mail Stop 148
  NASA Langley Research Center
  Hampton, VA 23681-2199

NASA/TM—2018-219988

Modeling-Driven Damage Tolerant Design of Graphene Nanoplatelet/Carbon Fiber/Epoxy Hybrid Composite Panels for Full-Scale Aerospace Structures

Julie M. Tomasi, William A. Pisani, Sorayot Chinkanjanarot, and Aaron S. Krieg
Michigan Technological University, Houghton, Michigan

Evan J. Pineda, Brett A. Bednarcyk, and Sandi G. Miller
Glenn Research Center, Cleveland, Ohio

Julia A. King, Ibrahim Miskioglu, and Gregory M. Odegard
Michigan Technological University, Houghton, Michigan

National Aeronautics and
Space Administration

Glenn Research Center
Cleveland, Ohio 44135

September 2018

Acknowledgments

The This research was partially funded by the I/UCRC on Novel High Voltage/Temperature Materials and Structures (Grant IIP-1362040), the Department of Mechanical Engineering - Engineering Mechanics at Michigan Tech, and the Richard and Elizabeth Henes Endowed Professorship at Michigan Tech. The authors also thank Collier Research Corp. HyperSizer for fruitful conversations and support regarding the structural-scale sizing performed in this study.

Level of Review: This material has been technically reviewed by technical management.

Available from

NASA STI Program
Mail Stop 148
NASA Langley Research Center
Hampton, VA 23681-2199

National Technical Information Service
5285 Port Royal Road
Springfield, VA 22161
703-605-6000

This report is available in electronic form at http://www.sti.nasa.gov/ and http://ntrs.nasa.gov/

Modeling-Driven Damage Tolerant Design of Graphene Nanoplatelet/Carbon Fiber/Epoxy Hybrid Composite Panels for Full-Scale Aerospace Structures

Julie M. Tomasi, William A. Pisani, Sorayot Chinkanjanarot, and Aaron S. Krieg
Michigan Technological University
Houghton, Michigan 49931

Evan J. Pineda, Brett A. Bednarcyk, and Sandi G. Miller
National Aeronautics and Space Administration
Glenn Research Center
Cleveland, Ohio 44135

Julia A. King, Ibrahim Miskioglu, and Gregory M. Odegard
Michigan Technological University
Houghton, Michigan 49931

Abstract

The objective of this study is to design a new nano graphene/carbon fiber/polymer hybrid composite that can be used for the NASA SLS Composite Exploration Upper Stage (CEUS) forward skirt structure. The new material will improve the resistance to open-hole compression failure of the structure relative to traditional polymer fiber composites. The material is designed rapidly and with little cost using the Integrated Computational Materials Engineering (ICME) approach. Multiscale modeling and experiments are used to synergistically optimize the material design to yield improved properties and performance by controlling key processing parameters for manufacturing nano-enhanced materials. Specifically, the nanocomposite panel showed a 22 percent reduction in mass relative to the traditional composite panel, while both designs are equal in terms of ease of manufacture. This potential mass savings corresponds to an estimated 45 percent savings in materials and manufacturing costs. The multiscale ICME workflow developed for this project can be readily applied to the development of nano-enhanced composite materials and large aerospace structures. In addition, all key aspects of ICME were employed to complete this project including multiscale modeling, experimental characterization and visualization, data management, visualization, error and uncertainty quantification, and education. The results presented herein indicate a dramatic level of success, as well as the power and potential of ICME approach and multiscale modeling for composite materials.

1.0 Introduction

Carbon/epoxy composite materials play a critical role in modern aerospace design. Their relatively high specific strength and specific stiffness make them ideal materials for lightweight structural components. While carbon/epoxy composites are already used in many current aerospace structures, continued material development is desired for improved mechanical performance. Specifically, it is desired to use composite laminates in the facesheets of sandwich panels used for the barrel section of launch vehicles, where open hole compression (OHC) strength is a key parameter that needs to be optimized to ensure damage tolerant designs (Refs. 1 and 2). Because large curved structures are subject to geometric imperfections and impact damage, the designs must utilize additional knockdown factors on top of the standard safety factor, as well as damage tolerant material properties. Thus, they can be overdesigned, and any increase in the OHC strength of the structure can yield significant weight savings.

Traditionally, the development of new composite materials has required a lengthy, iterative process of material formulation, specimen processing, testing and characterization, and formulation refinement. These steps are repeated until the desired properties are obtained. This is the known as the Edisonian approach to materials development, based on Thomas Edison's famous quote "I have not failed. I've just found 10,000 ways that won't work". Each iteration in the Edisonian approach can be relatively costly in terms of time, materials, and manpower. Integrated Computational Materials Engineering (ICME) promises to greatly facilitate the development of composite materials by cutting down on the number of iterations required to establish a composite material that meets design requirements. Because ICME provides an efficient means to explore materials design space, material properties can be optimized before specimens are processed and tested. Additionally, material processing can be linked to structural performance in an iterative and integrated manner.

Recently, Hadden et al. (Ref. 3) introduced a multiscale modeling method specifically designed for carbon fiber (CF)/epoxy composites that incorporates graphene nanoparticles (GNP) into the epoxy matrix for added stiffness. For these CF/GNP/epoxy hybrid composites, the modeling method included material characteristics of different length scales (nanoscopic and microscopic) to predict bulk-level elastic properties with a unidirectional CF orientation. It was found that the incorporation of GNP into the epoxy matrix has a significant impact on some of the elastic properties of the unidirectional hybrid composite. Furthermore, it was found that improvements in GNP dispersion could also have a strong effect on transverse properties. However, their study did not address nonlinear behavior of the material, such as OHC strength, or laminate architecture.

OHC strength of fiber-reinforced composite laminates is controlled by the shear response of the surrounding matrix (Ref. 4). As the laminate is loaded in compression, the fibers in the plies rotate which induces an increase in the shear strain. The elevation shear strain promotes microcracking in the matrix, degrading the shear stiffness. The reduction of the shear stiffness allows for additional rotation of the fibers. Thus, the fiber rotation, shear strain evolution, and matrix degradation are coupled and their effects are compounding. This ultimately leads to an instability failure during which a fiber kink band forms due to fiber microbuckling. Previous computational and experimental work has shown that the addition of GNP can increase the fracture toughness of epoxy materials (Ref. 5). A higher matrix toughness will improve the shear resistance, and thusly, the OHC strength of fiber-reinforced laminates.

Therefore, the objective of this study is to use state-of-the-art computational methods, along with some limited manufacturing and testing, for characterization and validation, to drive the development of a GNP/CF/epoxy material with enhanced OHC strength for integration into large, optimized, curved space structures. The improved stiffness from the addition of GNP will also improve buckling resistance of panels. However, in sandwich panel construction, the buckling resistance is most strongly influenced by the core thickness, so only minor buckling performance improvement can be gained from small increases in the facesheet stiffness. A combination of multiscale computational tools, including molecular dynamics (MD), micromechanics, the finite element method (FEM), and structural sizing, were implemented within a multiscale ICME workflow developed to achieve this objective, considering the thermoelastic and nonlinear mechanical response of the materials and structure. This ICME approach was performed at a fraction of the cost of traditional composite material development. The following parameters were included in the design space: GNP volume fraction, GNP dispersion, CF volume fraction, and composite laminate architecture. To establish the ICME workflow and a single set of these parameters was chosen to create an illustrative example.in which the OHC strengths were predicted, and an overall optimized full-scale structure was designed. The workflow demonstrated in this manuscript can be applied to the ICME of any aerospace structure containing GNP/CF/epoxy materials in which the design is driven by OHC strength. Furthermore, the workflow can be generalized so that it may accommodate other material and structural failure mechanisms. This paper will outline the collaboration between students, faculty, and researchers at Michigan Technological University and NASA Glenn Research Center to develop the optimized laminates. Also discussed is the business case and the technical results for this effort.

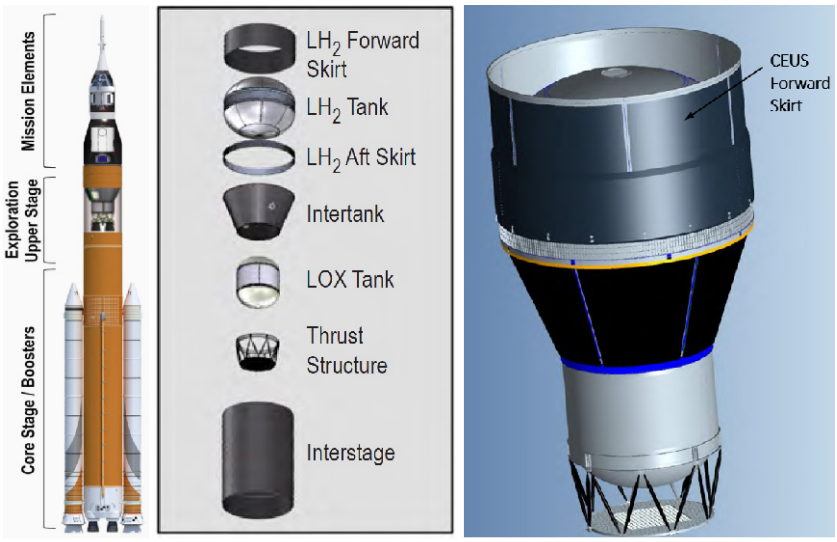

Figure 1.—Schematics of (a) the SLS Block 1B configuration, showing the location of the Exploration Upper Stage (Ref. 7), (b) an exploded view of the Exploration Upper Stage (Ref. 6), and (c) an assembled view of the Exploration Upper Stage, showing the forward skirt location (Ref. 6).

2.0 Skirt Structure of SLS Exploration Upper Stage

The structural scale application of this study that will be used to demonstrate improved structural performance, with the addition of GNP to the composite system, is the forward skirt structure of the SLS (Space Launch System) Exploration Upper Stage. The structure forms part of the main SLS rocket stack, as shown in Figure 1. While this structure is a relatively small part of the SLS vehicle, it is actually quite large, with a height of 1.778 m and a diameter of 8.4 m. This structure was chosen because it was recently the subject of a NASA structural concept trade study whose overarching goal was to examine infusion of composite materials, rather than traditional metallic construction, for the forward skirt structure in order to save mass (Ref. 6). This NASA project was called “Composites for Exploration Upper Stage” (CEUS), and the structural scale finite element model considered herein was developed as part of this project. As such, the structure is referred to throughout this paper as the CEUS forward skirt. After take-off, the CEUS forward skirt is subjected to a large bending moment resulting from the change in pitch of the rocket from the vertical direction. Aerodynamic loads and the payload mass introduces compressive stresses on one side of the skirt, possibly leading to failure.

3.0 Business Case

This project will ultimately provide a cost benefit for the manufacturer and users of the CEUS forward skirt. In particular, this project is focused on designing the damage tolerant facesheet laminates for the structural sandwich composites used on the skirt. The introduction of GNP into the carbon fiber composite facesheets can potentially increase the stiffness, strength, and toughness of the epoxy resin and thus increase the compressive strength of the facesheet laminate. This increase could lead to a reduction of the facesheet thickness and therefore a reduction in overall weight. Any reduction in weight ultimately leads to a significant cost savings in fuel, and reductions to the thickness lead to cost savings in manufacturing.

The ICME approach is ideal for this application because multiscale computational tools are available to establish structure-property relationships of fiber composites. With the combination of molecular dynamics, micromechanics, and finite element analysis; the influence of the molecular-sized GNP on the

bulk-level structural properties can be efficiently and accurately determined. The ICME approach described herein is augmented with a limited number of coupon experiments for model characterization and validation and to provide critical pieces of information to facilitate the material optimization. Gaps in physical test data are filled with heritage experimental data available in the literature, vendor data, or virtual data generated from simulation. Because the design is computationally-driven, the process is more efficient than the traditional Edisonian approach to composite material design.

Ultimately an overall weight savings of 22 percent was achieved, relative to a baseline design with no GNP, yielding a mass reduction of 47 percent in the facesheets. Assuming all designs use an "off the shelf" composite system, the manufacturing costs of the CEUS forward skirt are independent of the facesheet material and using quoted costs for the CF/epoxy pre-preg, GNP/CF/epoxy pre-preg and aluminum honeycomb core, (Refs. 8 and 9) the postulated mass savings would return a 45 percent savings in the cost of materials and manufacturing. Moreover, a reduction in structural mass yields an increase in the overall payload capability resulting in potential additional cost-savings.

4.0 Metrics for Success

A critical component of any ICME process is the clear definition of metrics for success. For this project, these are outlined here:

1. *Total cost of the facesheet laminate*. The project will be successful if the fabrication costs of the facesheet laminates used for the CEUS forward skirt sandwich composite panels can be reduced by 10 percent. The reduction in cost will come from the reduced thickness of the facesheets, and thus the reduction in total materials used and manufacturing effort to place or lay up the plies. The cost in GNP materials and manufacturing (including the extra resin mixing step) is minimal (<5 percent) compared to the savings associated with reducing the overall laminate thickness.
2. *Facesheet laminate weight*. The reduction in facesheet thickness will also lead to the reduction in structural mass of the CEUS forward skirt. The addition of GNP will thus lead to fuel savings associated with the launch.
3. *OHC strength*. This may be achieved by adjusting the GNP volume fraction, GNP dispersion, CF volume fraction, and laminate architecture. Increases in OHC will lead to reductions in facesheet laminate thickness, which lead to cost and weight savings.
4. *Development of ICME workflow*. Development of a multiscale modeling workflow which links measures of structural performance to processing and manufacturing parameters in an iterative and optimized framework.
5. *Partial completion of degree requirements*. Graduate students Julie Tomasi, Will Pisani, Sorayot Chinkanjanarot, and Aaron Kreig will include their work and results related to this project in their PhD dissertations.

5.0 Data Management and Collaboration Frameworks

The archiving and the exchange of data between researchers for this project was achieved using Google Drive and Google Docs. The material data obtained in this project will be provided to Granta MI (Ref. 10), which is a web-based system for materials information management. The pedigree of all data will be carefully tracked in terms of type (experimental, heritage, virtual), microstructure, software version, etc.

Experts from Michigan Tech University and NASA Glenn Research Center were assigned to particular experimental and modeling subtasks. These experts were responsible for the completion of their subtask and transition of the data or models generated into the greater workflow through Google Drive. Weekly team meetings were conducted via GoToMeeting.

6.0 Multiscale Modeling Methods

A multiscale modeling strategy was necessary to relate molecular structure and material microstructure to bulk-level nonlinear properties (i.e., OHC strength). An overview of the multiscale hierarchy employed in this work is depicted in Figure 2, and a description of each length scale is provided below.

- *Level 5*: *Nanoscale*. The lowest scale utilizes MD to predict the thermoelastic properties of GNP layers within an epoxy.
- *Level 4*: *Nanoscale Continuum*. Micromechanics and continuum damage mechanics (CDM) are used to calculate the nonlinear properties of GNP/epoxy.
- *Level 3*: *Microscale Matrix*. The nonlinear GNP/epoxy properties are homogenized over random orientations in 3-D).
- *Level 2*: *Lamina Scale*. Micromechanics and CDM are again used to calculate the effective nonlinear response of a CF/GNP/epoxy composite ply.
- *Level 1*: *Laminate Scale*. The OHC strength of CF/GNP/epoxy laminates is predicted using FEM and CDM.
- *Level 0*: *Structural Scale*. At the highest length scale, design of the full-scale space structure (CEUS) is completed with structural sizing and FEM software using OHC allowables calculated from the predicted OHC strengths at Level 1.

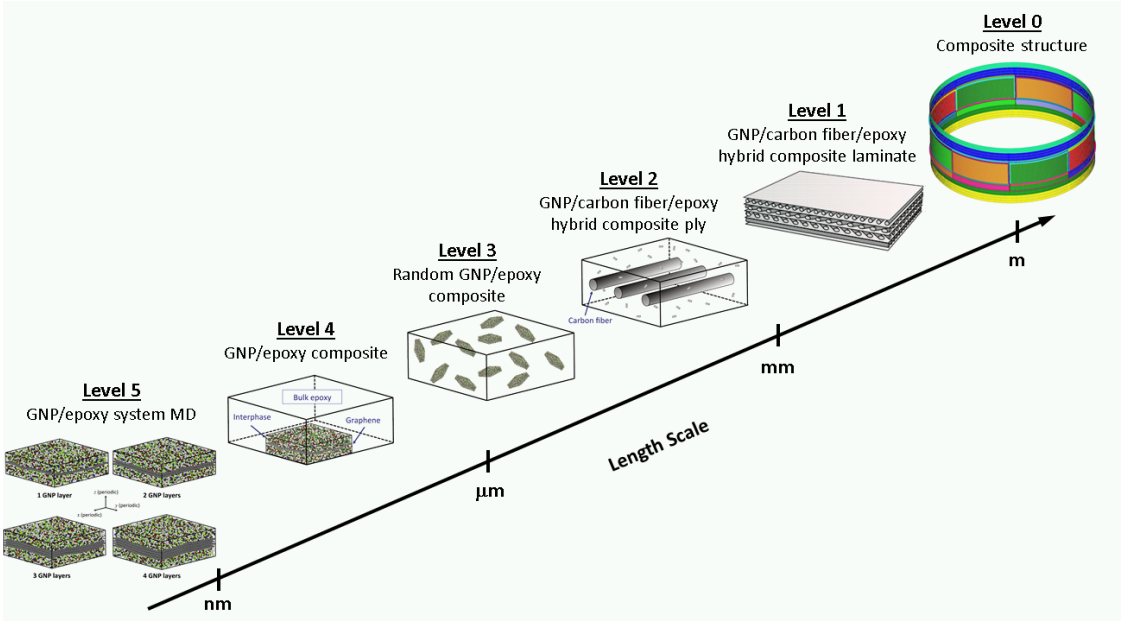

Figure 2.—Multiscale modeling hierarchy. Level 5: Nanoscale. Level 4: Nanoscale Continuum. Level 3: Microscale Matrix. Level 2: Lamina Scale. Level 1: Laminate Scale. Level 0: Structural Scale.

Flowcharts depicting the overall mechanical and thermal workflows are presented in Figure 3 and Figure 4, respectively. Different shapes and colors are used to represent different actions within the workflows. Rectangular boxes represent computational simulations, whereas rounded rectangular boxes indicate some type of characterization or validation procedure. Trapezoids depict some type of user input and the red color indicates that this is a material processing parameter. The parallelograms are data that is generated (black), used for characterization (blue) or used for valiation (purple). Finally, the green trapezoid is the performance data generated by the ICME workflow. Although only a single set of processing parameters is used in this current demonstration (Section 8.2), this workflow readily admits integration of material processing and performance in an iterative and optimized scheme. A wide range of computational tools and numerical methods are used throughout the developed ICME workflow and are underlined in the flowcharts in Figure 3 and Figure 4. Each of these are discussed in further detail throughout the following sections in hierarchical order, starting with the lowest length scale.

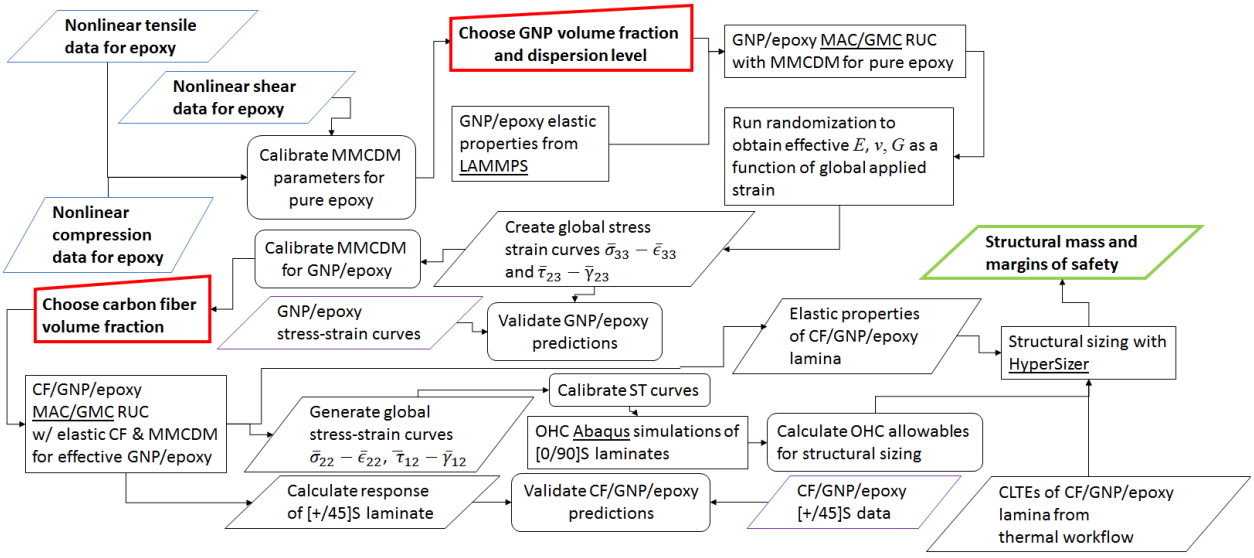

Figure 3.—Flowchart depicting multiscale modeling workflow for mechanical properties.

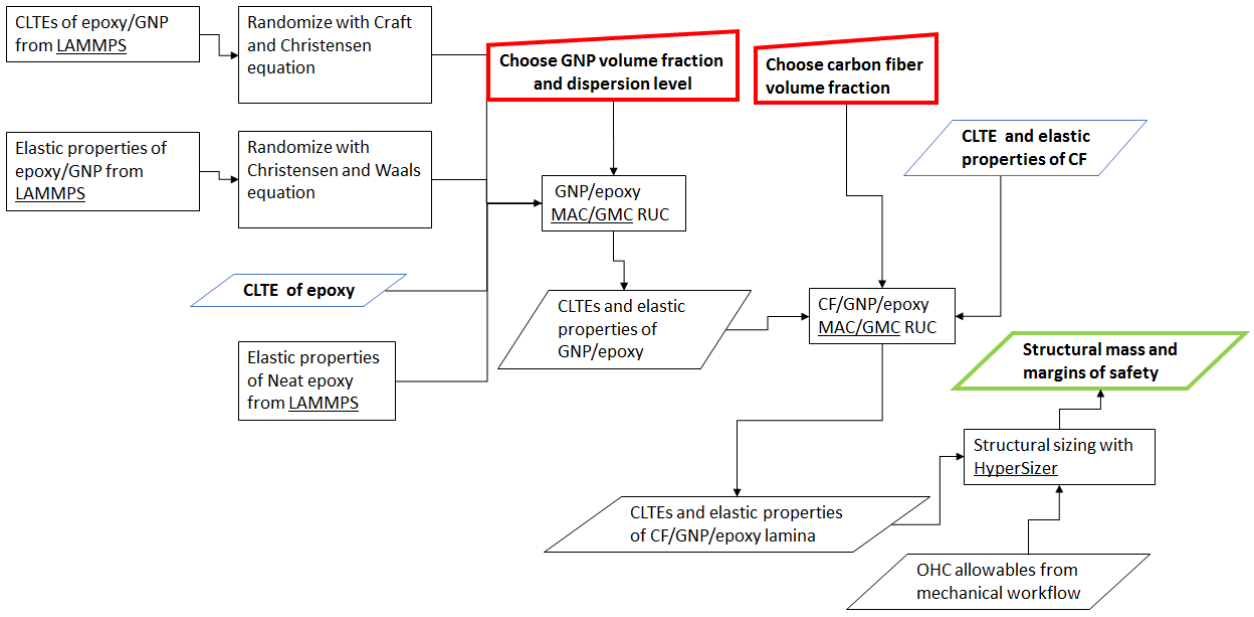

Figure 4.—Flowchart depicting multiscale modeling workflow for thermal properties.

6.1 Multiscale Modeling Workflow to Obtain OHC Strength of Notched CF/GNP/Epoxy Composite

6.1.1 Level 5: Molecular Dynamics Modeling of GNP/Epoxy

MD simulations are used to predict the thermoelastic properties and behavior of molecular systems on the nanometer length scale (Level 5). This is achieved by tracking the motion and interactions of individual atoms based on specified atomic potentials, molecular structure, and ambient conditions (specified pressure and/or temperature) (Ref. 11). MD simulations were carried out previously by Hadden et al. (Ref. 3) to predict the nano-scale elastic properties of molecular-scaled repeating unit cells (RUCs) of GNP and epoxy (Epon 862/DETDA system), as shown in Figure 5, Large-scale Atomic/Molecular Massively Parallel Simulator (LAMMPS) open source software (Ref. 12). Four different RUCs were simulated: with 1, 2, 3, and 4 layers of GNP. The 1-layer GNP model simulates a system with perfect GNP dispersion, while larger numbers of GNP layers represent systems with deceasing levels of dispersion. Dispersion is a facet of the manufacturing of the GNP/epoxy and GNP/CF/epoxy pre-preg. Improved dispersion indicates a more refined manufacturing process, but most likely comes at an added expense. For this project, dispersion is considered to be a material processing parameter. For each RUC, the full three-dimensional (3-D) elastic stiffness constants were determined. The full details for this analysis can be found elsewhere (Ref. 3).

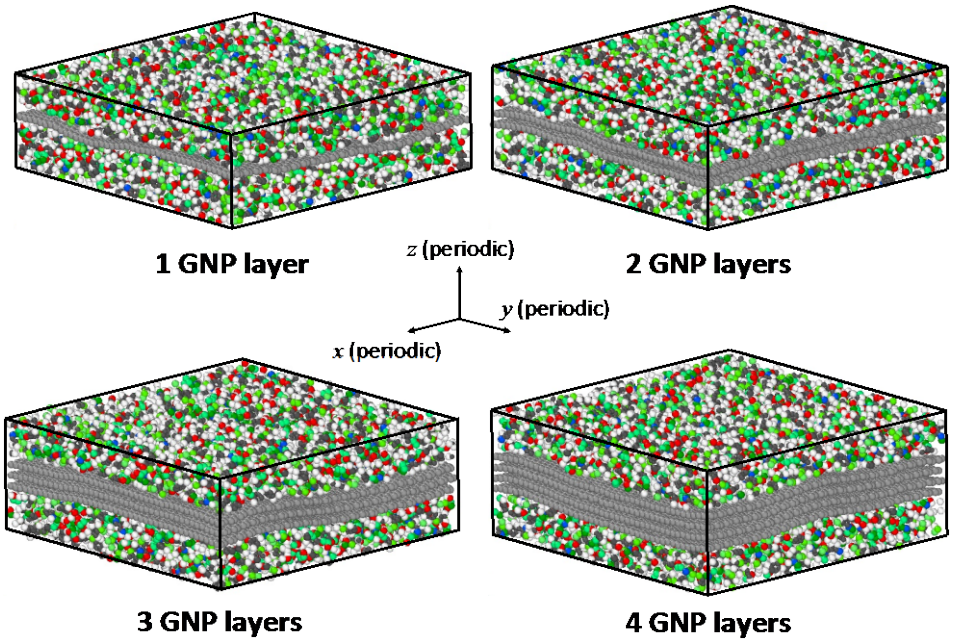

Figure 5.—Equilibrated MD models for varying number of graphene layers. The additional number of stacked graphene layers is indicative of poorer dispersion.

6.1.2 Level 4: Micromechanics Modeling of GNP/Epoxy

Micromechanics methods are continuum-based approaches that predict the bulk properties and nonlinear response of heterogeneous materials based on micro-structural morphology (e.g., reinforcing fiber volume fraction and orientation) and constituent properties. For this project, micromechanics models were established throughout the ICME workflow to ultimately predict the bulk mechanical and thermal properties of the CF/GNP/epoxy hybrid composites. The Generalized Method of Cells (GMC) micromechanics theory was used to provide the continuum-level predictions at Levels 4 and 2 (Refs. 13 to 15). With this method, an RUC representing the periodic material microstructure is identified. This RUC may contain as many constituent phases as is necessary to represent the composite material accurately. The RUC is discretized into a number of subcells, each of which is occupied by a single phase of the composite. Continuity of displacement and traction is enforced at each of the subcell interfaces, along with periodic boundary conditions, in an average (or integral) sense, to arrive at a strain concentration matrix. Once the strain concentration matrix is obtained, the local subcell stresses and strains, and the homogenized RUC stiffness tensor, can be readily obtained. The semi-analytical procedure is extremely computationally efficient and provides nonlinear solutions on the order of seconds, or less. For the research presented herein, the MAC/GMC software package implementation of GMC, developed by the NASA Glenn Research Center (Ref. 16), was used.

Level 4 modeling of a GNP/epoxy RUC containing GNP layers at a single orientation, where the stacking direction of the GNP is aligned with the $x_3^{(4)}$-direction, was accomplished using MAC/GMC and shown in Figure 6. This scale is needed to bridge the gap between the molecular and continuum scales to ensure that the volume fraction of GNP in the epoxy is appropriate and consistent with the actual material. The triply periodic 2×2×2 RUC consists of a single GNP/epoxy subcell, shown in yellow in Figure 6, and seven pure epoxy subcells, colored green. Since the MD model contains both GNP and epoxy, at the relative GNP volume fractions $v_{GNP}^{(5)}$ were used. To obtain the correct volume fraction of GNP that is representative of the amount of GNP within the matrix $v_{GNP}^{(4)}$, the volume fraction of the effective GNP/epoxy subcell $v_{GNP/Epoxy}^{(4)}$ in the Level 4 RUC must be calculated appropriately:

$$v_{GNP/Epoxy}^{(4)} = \frac{v_{GNP}^{(4)}}{v_{GNP}^{(5)}} \tag{1}$$

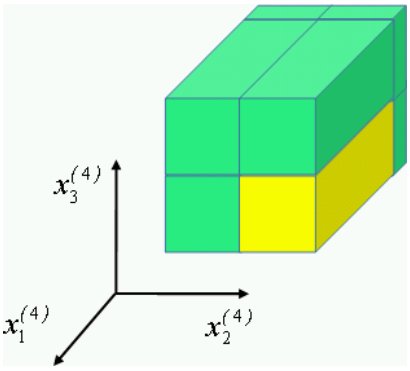

Figure 6.—Level 4 MAC/GMC GNP/epoxy RUC containing an elastic subcell with GNP/epoxy properties from MD (yellow), and pure epoxy subcell (green) modeled with MMCDM.

One goal of the analysis workflow is to predict the OHC strength of hybrid CF/GNP/epoxy composites. As such, material nonlinearity must be included within the multiscale analysis workflow. Since the MD simulations were only used to predict the linear response of GNP/epoxy and the overall volume fraction of GNP in the epoxy $v_{GNP/Epoxy}^{(4)}$ is low, the GNP/epoxy subcell is also considered to be elastic using the properties from MD. However, nonlinearity due to damage was incorporated into the pure epoxy subcells using the Multiaxial Mixed-mode Continuum Damage Mechanics (MMCDM) model (Ref. 17), and the nonlinear homogenized response of the Level 4 RUC is realized using GMC.

MMCDM utilizes a nonlinear relationship between an effective damage stress and an effective damage strain. It is assumed that damage growth is planar, representing microcracking. The effective damage stress and strain are normalized, coupled measures of the normal and shear stress and strain components that would promote crack growth normal to one of the material coordinate system directions. Damage initiates when the effective damage strain exceeds a value of one, and the normalized tangent stiffness of the effective damage stress-strain curve is an exponential function of the effective damage strain. MMCDM accommodates a different response in tension and compression. In addition, normal damage and shear damage between are coupled, and a set of weight parameters can be used to control this coupling. The full mathematical formulation of MMCDM is detailed elsewhere (Ref. 17). The input parameters for MMCDM are calibrated against heritage experimental data from the literature (Section 8.2).

MMCDM was chosen to model the nonlinear response of the epoxy subcells in the Level 4 and Level 2 GMC models for multiple reasons. First, it is assumed that nonlinearity within the resin is a result of accumulating microcracks. MMCDM utilizes concepts from fracture mechanics to couple the degradation of the normal and shear engineering constants of the material. In addition, MMCDM is suitable for modeling damage growth due to microcracking in an initially isotropic medium. As damage accumulates, the stiffness tensor does not remain isotropic because degradation of the components of the stiffness tensor are directional, based upon the orientation of the micorcracks. The GMC theory employs a full 3-D stress and strain formulation. Since MMCDM is also formulated in full 3-D, it is amenable for implementation within GMC. Finally, MMCDM has been validated, used to predict the nonlinear stress-strain response of fiber-reinforced laminates, and is implemented within the latest distribution of MAC/GMC (Version 4z.3-7) (Refs. 17 and 18).

6.1.3 Level 3: Homogenization of Randomly Oriented GNP in Epoxy

As stated previously, the RUC presented in Figure 6 represents layers of GNP within epoxy oriented at a single orientation. More realistically, the orientation of GNP within the epoxy is random because of the manufacturing process, as shown in Figure 2, Level 3. To obtain the nonlinear response of GNP/epoxy with randomly oriented GNP, the homogenization procedure of Christensen and Waals (Ref. 19) is extended to consider nonlinear materials in this work.

The components of the Level 3 stiffness tensor $C_{33}^{(3)}$, $C_{23}^{(3)}$ of an RVE containing an arbitrarily oriented Level 4 RUC can be calculated by assuming only a single Level 3 (i.e., global) normal strain component $\bar{\varepsilon}_{33}^{(3)}$ is applied in the $x_3^{(3)}$-direction following Christensen and Waals (Ref. 19).

$$C_{33}^{(3)} = \bar{C}_{11}^{(4)}\cos^4\theta + \left(2\bar{C}_{12}^{4} + 4\bar{C}_{66}^{4}\right)\cos^2\theta\sin^2\theta + \bar{C}_{22}^{(4)}\sin^4\theta \tag{2}$$

$$\begin{aligned} C_{23}^{(3)} = {} & \left(\bar{C}_{11}^{(4)} + \bar{C}_{22}^{(4)} - 4\bar{C}_{66}^{(4)}\right)\cos^2\theta\sin^2\theta\sin^2\varphi \\ & + \bar{C}_{12}^{(4)}\left(\sin^4\theta\sin^2\varphi + \cos^4\theta\sin^2\varphi + \cos^2\theta\cos^2\varphi\right) \end{aligned} \tag{3}$$

where $\bar{C}_{ij}^{(4)}$ are components of the effective Level 4 RUC stiffness tensor, and θ and ϕ are angles relating the two coordinate systems in spherical coordinates, defining the directional cosines. The components of the effective Level 3 stiffness tensor, $\bar{C}_{33}^{(3)}$, $\bar{C}_{23}^{(3)}$, containing completely randomly oriented Level 4 RUCs, are determined by averaging Equations (2) and (3) over all possible orientations:

$$\bar{C}_{33}^{(3)}\left(\bar{\varepsilon}_{33}^{(3)}\right)=\frac{1}{2\pi}\int_0^{2\pi}\int_0^{2\pi}C_{33}^{(3)}\left(\bar{\varepsilon}^{(4)},\theta,\varphi\right)\sin\theta d\theta d\phi \tag{4}$$

$$\bar{C}_{23}^{(3)}\left(\bar{\varepsilon}_{33}^{(3)}\right)=\frac{1}{2\pi}\int_0^{2\pi}\int_0^{2\pi}C_{23}^{(3)}\left(\bar{\varepsilon}^{(4)},\theta,\varphi\right)\sin\theta d\theta d\phi \tag{5}$$

The behavior of the Level 4 RUC is nonlinear. Thus, the components of the effective Level 3 stiffness tensor, $\bar{C}_{33}^{(3)}$, $\bar{C}_{23}^{(3)}$, are functions of the applied strain, $\bar{\varepsilon}_{33}^{(3)}$. The stiffness components of the Level 3 RVE containing an arbitrarily oriented Level 4 RUC are implicitly dependent on the effective applied strain in the Level 4 coordinate system $\bar{\varepsilon}^{(4)}$. This relationship cannot be determined analytically because it is a result of the GMC homogenization. Therefore, the averaging Equations (4) and (5) are converted into summations, and an approximation of the components of the nonlinear homogenized stiffness tensor at Level 3, $\tilde{C}_{33}^{(3)}$, $\tilde{C}_{23}^{(3)}$, are given:

$$\tilde{C}_{33}^{(3)}\left(\bar{\varepsilon}_{33}^{(3)}\right)=\frac{\Delta\theta\Delta\varphi}{2\pi}\sum_{m=1}^{2\pi/\Delta\varphi}\sum_{n=1}^{2\pi/\Delta\theta}C_{33}^{(3)}\left(\bar{\varepsilon}^{(4)},n\Delta\theta,m\Delta\varphi\right)\sin\left(n\Delta\theta\right) \tag{6}$$

$$\tilde{C}_{23}^{(3)}\left(\bar{\varepsilon}_{33}^{(3)}\right)=\frac{\Delta\theta\Delta\varphi}{2\pi}\sum_{m=1}^{2\pi/\Delta\varphi}\sum_{n=1}^{2\pi/\Delta\theta}C_{23}^{(3)}\left(\bar{\varepsilon}^{(4)},n\Delta\theta,m\Delta\varphi\right)\sin\left(n\Delta\theta\right) \tag{7}$$

where Δθ and Δϕ are the increments in orientation used in the summation, and the results of Equations (6) and (7) are sensitive to these parameters. Note, it is also possible to solve Equations (4) and (5) through numerical integration.

The elastic response of an epoxy RVE containing randomly oriented GNPs is isotropic. This does not account for agglomeration of the GNP within the epoxy. Further investigation would be needed to determine the effect of GNP clustering on the properties of the GNP. It is assumed here that isotropy holds in the nonlinear regime when the matrix is damaged. As such, the nonlinear engineering constants $\tilde{E}^{(3)}$ (Young' modulus), $\tilde{v}^{(3)}$ (Poisson's ratio), and $\tilde{G}^{(3)}$ (shear modulus) can be calculated using,

$$\tilde{v}^{(3)}=\frac{\tilde{C}_{23}^{3}}{\tilde{C}_{33}^{3}+\tilde{C}_{23}^{3}} \tag{8}$$

$$\tilde{E}^{(3)}=\frac{\tilde{C}_{33}^{(3)}\left(1+\tilde{v}^{(3)}\right)\left(1-2\tilde{v}^{(3)}\right)}{\left(1-\tilde{v}^{(3)}\right)} \tag{9}$$

$$\tilde{G}^{(3)}=\frac{\tilde{E}^{(3)}}{2\left(1+\tilde{v}^{(3)}\right)} \tag{10}$$

The assumption that isotropy is retained as damage evolves locally at Level 4 may be a source of error because the MMCDM model assumes damage is due to matrix cracking and degrades the components of the stiffness tensor in anisotropic manner. Moreover, the presence of an elastic inclusion also yields anisotropic nonlinearity. Homogenization of Level 3 is performed using Equations (6) to (10) to obtain the effective nonlinear uniaxial normal and shear stress-strain response for each applied strain increment assuming a secant relationship,

$$\overline{\sigma}_{33}^{(3)} = \tilde{E}^{(3)}\overline{\varepsilon}_{33}^{(3)}; \qquad \overline{\varepsilon}_{11}^{(3)} = \overline{\varepsilon}_{22}^{(3)} = \overline{\gamma}_{23}^{(3)} = \overline{\gamma}_{13}^{(3)} = \overline{\gamma}_{12}^{(3)} = 0 \tag{11}$$

$$\overline{\tau}_{23}^{(3)} = \tilde{G}^{(3)}\tilde{\gamma}_{23}^{(3)}; \qquad \overline{\varepsilon}_{11}^{(3)} = \overline{\varepsilon}_{22}^{(3)} = \overline{\varepsilon}_{33}^{(3)} = \overline{\gamma}_{13}^{(3)} = \overline{\gamma}_{12}^{(3)} = 0 \tag{12}$$

6.1.4 Level 2: Micromechanics Modeling of CF/GNP/Epoxy

The nonlinear response of a unidirectional CF/GNP/epoxy ply is predicted using MAC/GMC at Level 2. The single-fiber RUC, representing a square-packed fiber architecture is displayed in Figure 7. The elastic CF subcells are shown in blue. The red subcells represent homogenized epoxy with randomly oriented GNP. The nonlinear behavior of these subcells is captured with MMCDM. The effective elastic properties are obtained from, and the MMCDM parameters are calibrated using, Level 3 simulations. Uniaxial stress-strain results are used for the calibration of the MMCDM parameters, and it is assumed that the MMCDM parameters are not directionally dependent. If initiated, the evolution equations governing stiffness degradation are the identical for the three different Level 2 directions $x_i^{(2)}$. However, the strains associated with development of microcacks normal to a particular direction must satisfy a damage initiation criterion, and only particular components of the stiffness tensor are degraded to simulate microcrack growth. Therefore, damage evolution is anisotropic. However, some error may still be retained from the assumption that the isotropic relationship between the Young's modulus, Poisson's ratio, and shear modulus holds (Eq. (10)); this assumption must be verified, or the error resulting from it should be quantified.

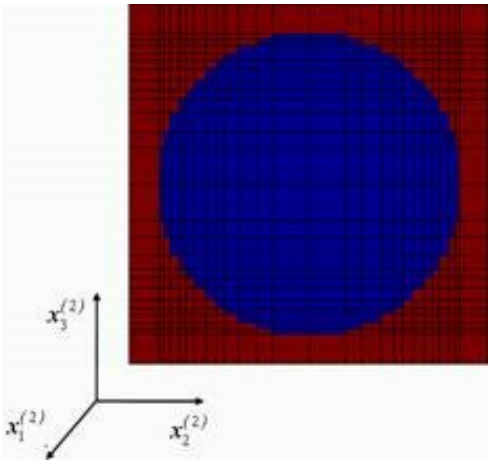

Figure 7.—Level 2 MAC/GMC GNP/epoxy RUC containing elastic subcells with CF (blue), and subcells representing epoxy with randomly oriented GNPs (red) modeled with MMCDM.

6.1.5 Level 1: Finite Element Modeling of Open Hole Compression of CF/GNP/Epoxy Laminates

At Level 1, OHC simulations are performed using the Abaqus FEM software package. The FEM model is shown in Figure 8. The dimensions of the OHC specimen, given in Figure 8(a), were chosen based up the ASTM D6484/D6484M for obtaining OHC allowables for polymer matrix composites (PMCs) (Ref. 20). The OHC specimen model is 100 mm long and 38 mm wide with a hole placed at the center with a radius of 3 mm. The requirements for the laminate stacking sequence, given in the ASTM standard, are that the laminate is multidirectional, with fibers oriented in a minimum of two directions, the layup is balanced and symmetric, and the nominal thickness is 4 mm with an allowable range of 3 to 5 mm. As such, the OHC specimen model consists of a $[0n/90n]_S$ stacking sequence and a total thickness of 4 mm. The fiber orientation angle in the stacking sequence is relative to the $x_1^{(1)}$ -direction shown in Figure 8.

The FEM mesh used to discretize the OHC specimen is displayed in Figure 8(b). The mesh consists of 5,915 two-dimensional (2-D), plane stress, reduced integration, quadrilateral, layered shell S4R elements, totaling to of 6,027 nodes and 36,162 degrees of freedom (DOFs). Three through thickness integration points are utilized in each shell layer, yielding a total of 12 through thickness integration points per element. Figure 8(c) shows the gage section that is 25 mm long. The refined mesh in the gage section was chosen after a mesh convergence study based on the global nonlinear response of the OHC specimen.

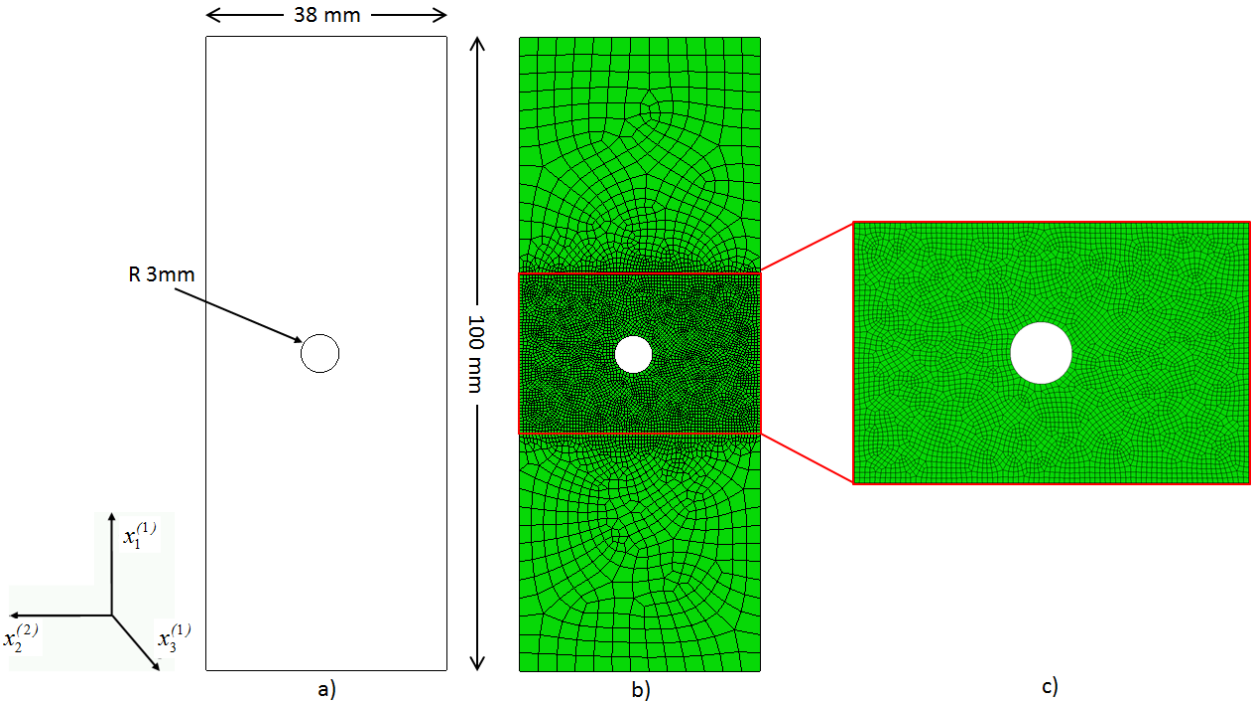

Figure 8.—OHC FEM model. (a) Geometry of OHC specimen based on ASTM D6484/D6484M. (b) FEM mesh. (c) Exploded view of refined FEM mesh in gage section.

The domain shown in Figure 8 depicts the volume of the specimen between the grips in the OHC test fixture. The effect of the grips is modeled through the end boundary conditions. The bottom edge is clamped and all six DOFs are constrained. At the top edge, all DOFs are constrained except for displacement in the $x_1^{(1)}$ -direction. The OHC test fixture is composed of long grips that prevent out-of-plane buckling of the test specimen. To mimic this, the displacement in the $x_3^{(1)}$ -direction for all nodes is constrained.

The OHC test is simulated using Abaqus/Explicit. A uniform edge displacement of 3 mm is applied in the $x_1^{(1)}$ -direction over a duration of 10 sec to simulate the introduction of a compressive load through the gripped area. Mass scaling is introduced every 1000 increments to increase the minimum stable time increment to 0.001 sec. Finally, geometric nonlinearity is considered in the analysis.

A primary compressive mode of failure for fiber-reinforced PMCs is formation of a kink-band due to fiber microbuckling (Refs. 4, 20 to 22). To model kink-band formation, all integration point calculations are performed in the instantaneous fiber frame, which is tracked using the deformation gradient (Refs. 21 and 22). As the local transverse and shear moduli begin to degrade due to matrix damage, there is less resistance to fiber rotation. In turn, fiber rotation promotes further degradation of the transverse and shear properties. Eventually, this leads to a runaway instability and a kink band forms.

Simulation of Level 1 damage mechanisms are limited to matrix microdamage and fiber microbuckling. Ply level matrix microdamage is modeled using the thermodynamically-based work potential theory, coined Schapery theory (Refs. 22 to 24). An internal state variable (ISV), S_r, is utilized as a measure of the energy dissipated through the advancement of matrix microdamage. Microdamage is considered to be the culmination of subcritical damage mechanisms, such as microcracking, shear banding, micro-void growth, and fiber-matrix debonding, that result in a nonlinear response of a composite ply up to the onset of more severe damage or failure mechanisms (i.e., transverse cracking, delamination and/or fiber rupture). This is appropriate for this example since fiber microbuckling is driven by shear degradation of the matrix and rotation of the fibers. Microdamage results in a strain hardening response of the composite ply. Failure, which produces strain softening and localization, is not considered in this analysis. Therefore, no energy regularization techniques are required to eliminate the pathological mesh dependence that is observed within FEM when there is strain localization. ST has been previously validated for predicting the strain-hardening response, due to microdamage evolution, of numerous simple laminates (Refs. 24 and 25).

ST and the fiber microbuckling model are available within NASA's Enhanced Schapery Theory (NEST) progressive damage and failure analysis (PDFA) tool, which is implemented into the Abaqus/Explicit FEM software through a VUMAT user subroutine and based upon previous work by Pineda and Waas (Ref. 26). The primary nonlinear inputs for NEST are a set of three microdamage polynomial functions, which relate the transverse and shear ply properties to the ISV under transverse tension, transverse compression and shear strain loading. At Level 1, these polynomial functions are calibrated to match the output results from the Level 2 micromechanics simulations, which employed MMCDM to model damage in the matrix. ST was chosen to model matrix microdamage at this scale, as opposed to MMCDM, because ST is formulated for transversely isotropic homogenized macroscopic fiber-reinforced PMC plies, whereas MMCDM was developed for matrix constituents. In addition, ST assumes a plane stress state, allowing for FEM modeling with shell elements resulting in improved computational efficiency. This trade-off for speed over accuracy is becoming of an ICME project because run-times for full 3-D, nonlinear FEM models are lengthy (even on multiple processors), and multiple FEM simulations may be needed in an ICME workflow. In addition, ST has been used to successfully predict the nonlinear behavior of the tension and compression of notched laminates (Refs. 27 and 28). Finally, it has been previously demonstrated that GMC with MMCDM can effectively be used to predict the lamina-scale ST microdamage functions (Ref. 18). NEST was used to perform the PDFA of the OHC specimen and predict the OHC strength of the specimen, which is then used to calculate the OHC allowables utilized in the Level 0 structural design.

6.2 Multiscale Modeling Workflow for Thermal Properties

GNP/EPON862 modeled by Hadden et al. (Ref. 3) with all four levels of dispersion were used for this analysis. The 80 percent crosslinking models were selected as most realistic. The models were equilibrated by using the NPT (constant pressure and temperature) ensemble with the "aniso" type of barostat (as implemented in LAMMPS) at 1 atmosphere and 300 K. The equilibration ran for 2 ns with 1 fs timesteps. The cut-off radius for airwise interactions was set at 10 angstroms. All equilibrated models were prepared by reducing the temperature to 173 K in the NPT ensemble with the aniso type of barostat set at 1 atmosphere. This preparation ran for 500 ps with 1 fs timesteps. Subsequently, simulations were performed with two different methods (heating-up and cooling-down) to determine the coefficient of linear thermal expansion (CLTE). The heating-up method continued from the preparation step by heating from 173 K up to 800 K using the NPT ensemble with aniso at 1 atmosphere for 5 ns with 1 fs timesteps. The cooling-down method was continuously applied after the heating up method by decreasing the temperature from 800 to 173 K with the same settings and simulation time. The temperatures and box lengths on each direction were individually averaged every 2 ps and exported to a log file. The CLTE was calculated using,

$$\alpha = \frac{1}{\delta T}\frac{\delta L}{L} = \frac{1}{L}\frac{\delta L}{\delta T} \tag{13}$$

The randomized CLTEs of the GNP/epoxy models were calculated using the equation by Craft et al. (Ref. 29)

$$\alpha_r = \frac{\left[E_{11} + 4\nu_{12}\left(1+\nu_{12}\right)K_{23}\right]\alpha_1 + 4\left(1+\nu_{12}\right)K_{23}\alpha_2}{E_{11} + 4\nu_{12}\left(1+\nu_{12}\right)K_{23}} \tag{14}$$

The elastic properties in Equation (14) were taken from the modeling results discussed below.

MAC/GMC was used to determine the CLTE of the homogenized GNP/epoxy composite. A triply periodic 2×2×2 RUC (cubic packing array), shown in Figure 6 was employed, with the aspect ratio equal to 1. The randomized CLTE of GNP/epoxy was applied as the inclusion region (yellow subcell in Figure 6). The Christensen and Waals equations (Ref. 19) were applied to the elastic properties obtained from MD to determine the elastic properties of a system containing GNP/epoxy at completely random orientations, following the work of Hadden et al. (Ref. 3) The elastic modulus (2.72 GPa) and properties Poisson's ratio (0.43) of the pure epoxy are from previous studies (Ref. 30) and Little et al., (Ref. 31) respectively. The shear modulus was calculated by Equation (15) equal to 0.951 GPa and the CLTE [α = 86 ppm/°C] of the pure epoxy was taken from the work of Bandyopadhyay et al. (Ref. 32) The volume fraction of the subcell containing the properties from the randomization of the MD results was calculated using Equation (1) to provide a consistent overall GNP volume fraction in the RUC.

It should be noted that there is a difference between the workflow for obtaining the CLTE properties, and the workflow used to calculate the nonlinear mechanical properties. For the CLTE, the randomization of the GNP/epoxy occurs immediately after the MD calculations, and the randomized MD CLTEs are used in the micromechanics model of the GNP/Epoxy RUC. This workflow is analogous to that demonstrated by Hadden et al. (Ref. 3) To arrive at the nonlinear mechanical properties, the elastic properties from MD are used directly in the GNP/epoxy RUC micromechanics model and the nonlinear results from simulations at multiple orientations are averaged to obtain the effective nonlinear mechanical properties of a GNP/epoxy material with randomly oriented GNP. This method is similar to that presented by Klimek-McDonald et al. (Ref. 33). Although the multiscale homogenization procedure developed in Klimek-McDonald (Ref. 33) more closely represents the effective RVE containing randomly oriented GNPs distributed throughout an epoxy matrix, the error introduced when calculating the effective CLTE for the GNP/epoxy composite should be minimal because these properties are linear and mainly a function of the volume fraction of the constituents, and the overall orientation distribution of the inclusion.

6.3 Structural Modeling and Simulations

Structural design simulations were performed using the HyperSizer Structural Sizing Software (Ref. 34), along with the MSC/NASTRAN finite element solver (Ref. 35), with the intent of determining a realistic, optimized, manufacturable design for the SLS CEUS forward skirt. The finite element model employed, which was developed by NASA for structural concept trade studies (Ref. 6), is shown in Figure 9. The model includes the forward skirt composite panels, along with load introduction structure and metallic frames adjacent to the forward skirt (consisting of metallic facesheet sandwich panels and the beams shown in Figure 9). The load introduction and adjacent metallic frame structures are intended to enable the applied loads to be transferred to the CEUS forward skirt panels in a realistic manner, while also approximately accounting for the stiffness of the forward and aft structure to which the CEUS forward skirt is attached. The designs of these structures have been set and thus, while they are present in the finite element model, they were not sized as part of the CEUS composite panel design. The composite panel portion of the CEUS forward skirt is 1.778 m (70 in.) long and has a diameter of 8.4 m.

As shown in Figure 9, there are longitudinal C Beams present in the finite element model that divide the CEUS forward skirt into eighths. The locations of these beams are intended to correspond to the location of joints between one-eighth panels, which would be manufactured independently and assembled to form the CEUS forward skirt. The size of these one-eighth panels is 1.778×3.3 m (5.8×7 in.), and they can thus be processed in many available autoclaves (as opposed to larger sections, which would require larger, less common autoclaves). The panels that comprise the one-eighth sections of the CEUS forward skirt have been subdivided into components and then grouped for sizing. The groups employed in the sizing process are shown in Figure 10. As shown, these groups are composed of multiple panels from around the CEUS circumference. Each panel is sized independently based on its local loads, but the panel designs within a given group have been linked so that all panels within the group have the same design. This design must pass all failure criteria checks for every load case for every panel. This linking is necessary because the load cases (discussed below) have not been “clocked” circumferentially around the structure. Thus, without the linking, the panel design would vary significantly circumferentially, and if the vehicle rotated off of the assumed loading orientation during launch, a different section of the structure would be placed under the most severe compressive loads, likely causing failure. By linking the designs within the groups, each one-eighth section of the structure will have an identical design, avoiding the need to consider multiple orientations per load case and simplifying the manufacturing of the structure.

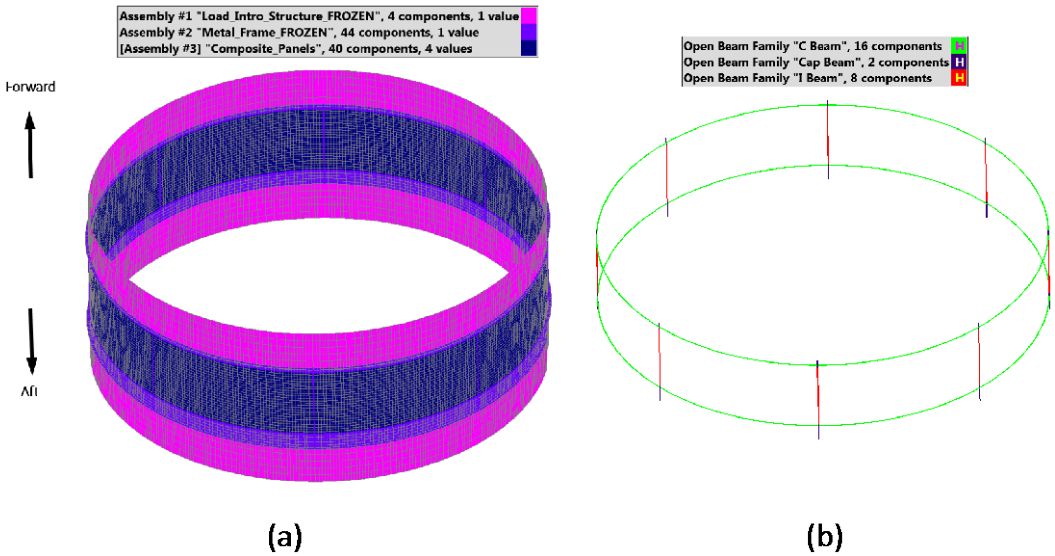

Figure 9.—(a) Structural finite element model of the CEUS. (b) Beam elements included in the model (part of the Metal Frame Assembly).

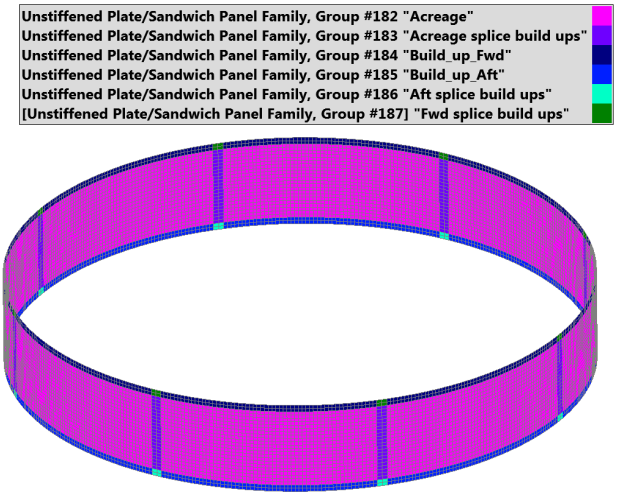

Figure 10.—Sizing groups, which have been required to have the same design, employed in the sizing process.

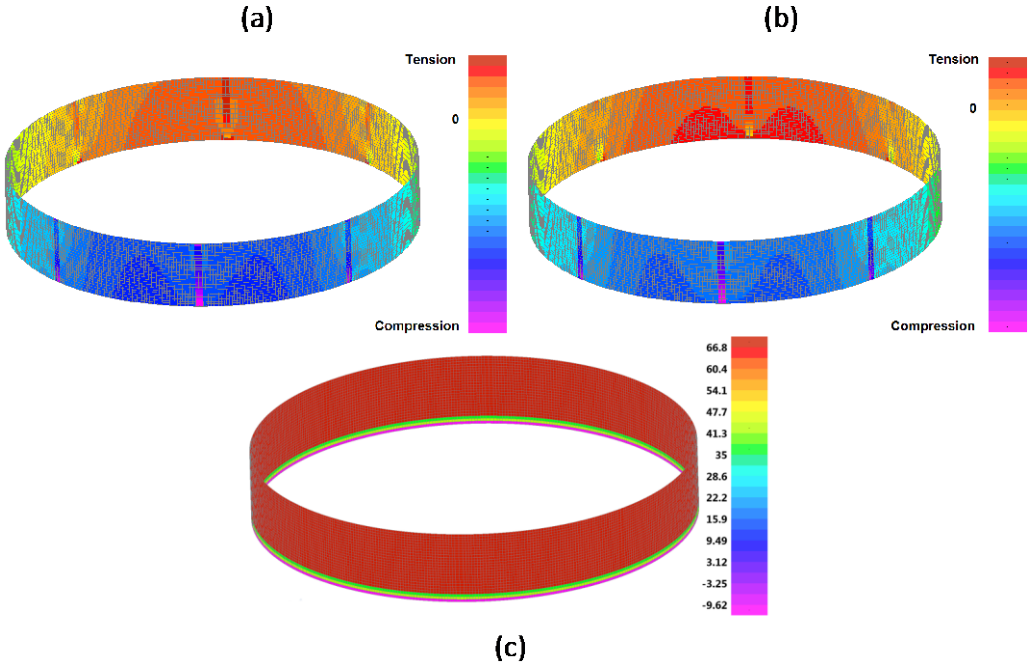

Figure 11.—Example longitudinal (N_x) force resultant distributions in the CEUS forward skirt composite panels due to (a) flight loads plus burst pressure and thermal loading and (b) flight loads plus crush pressure and thermal loading. (c) Temperature distribution (°F) applied to the CEUS forward skirt composite panels to do the proximity to the liquid hydrogen tank.

Two load cases have been considered in the CEUS forward skirt design, one representing SLS flight loads plus burst pressure, and one representing SLS flight loads plus crush pressure. Both of these mechanical load cases are paired with a thermal load case that results from the adjacent metallic liquid hydrogen tank (Figure 1). Details of this loading are not publicly releasable, but, as would be expected in a launch vehicle structure such as the CEUS forward skirt; the loading is compression dominated, with additional bending and shear loading from the aerodynamic loads on the rocket during flight. Figure 11 gives a qualitative sense of the longitudinal (N_x) stress resultants that drive the CEUS forward skirt composite panels, along with temperature imposed on the structure. The location of zero force is indicated in Figure 11(a) and (b), showing that one side of the structure is in compression, while the other is in

tension, but the magnitude of the compressive forces is much higher. Also, the locations of the splice build ups at the joints between the one-eighth segment panels are apparent due to their higher structural stiffness compared to the acreage. As mentioned, the loading has not been clocked around the CEUS forward skirt circumference, but the linking of the one-eighth panel designs ensures that the structure is designed to withstand any orientation of the applied loading.

Standard ultimate factors of safety have been used in the composite panel sizing. A 1.4 factor of safety was used for the acreage while, for the build ups, which represent discontinuities in the structure, a factor of safety of 2.0 has been employed. For panel buckling, an additional buckling knockdown factor of 0.65 was employed. HyperSizer's two sigma statistical processing method (Ref. 34) has been used within the software to arrive at the panel design-to loads from the element level loads produced by the finite element solver. In addition, HyperSizer's default aerospace composite failure criteria checks have been employed in the sizing, with the exception of strain-based strength criteria. As discussed below, emphasis was placed in the present study on developing stress allowables for the considered material systems, rather than strain allowables, so strain-based failure checks were disabled. Therefore, the ply-level material strength failure criteria considered were: max stress, Tsai-Hill, Tsai-Wu, Tsai-Hahn, Hoffman, and LaRC03. The sandwich panel specific failure criteria considered were: flatwise tension, core shear strength, facesheet wrinkling, core shear crimping, intracell dimpling, and core crushing. Finally, panel buckling failure was considered based on HyperSizer's buckling energy solution for curved panels, along with independent finite element global buckling eigenvalue solutions. Details on HyperSizer's failure criteria methods are available from the product website (Ref. 34).

7.0 Experimental Methods

As part of the ICME process, experimental tests are critical for both model validation and providing key data for characterizing the models. In this section the specimen fabrication and testing methods are discussed.

7.1 Materials

The resin and hardener used in this study are EPON 862 (diglycidyl ether of bisphenol F, DGEBF) and EPIKURE Curing Agent W (diethyltoluenediamine, DETDA). EPON 862 is a low-viscosity, liquid epoxy resin manufactured from epichlorohydrin and Bisphenol-F9. The viscosity of EPON 862 and EPIKURE Curing Agent W at 25 °C is 35 P and 200 cP, respectively (Ref. 3). This epoxy system is available from Momentive Specialty Chemicals, Inc. The graphene nanoplatelet (GNP) used in this study is xGnP® C-300 from XG Sciences. xGnP-C-300 has an average particle diameter of 2 mm, a thickness of 2 nm, a density of 2.0 g/mL, and a surface area of 300 m^2/g (Ref. 36). The continuous carbon fiber used in this study is Hexcel HexTow® AS4 3K. AS4 is a continuous PAN-based fiber with a high strength and high failure strain. AS4 has a density of 1.79 g/mL and a longitudinal modulus of 231 GPa (Ref. 37). The fiber was surface treated and sized (1 wt% sizing) (Ref. 37).

7.2 Specimen Fabrication

7.2.1 Baseline GNP/Epoxy

For the baseline panel, which consists of only epoxy and carbon fiber (i.e., no GNP), a ratio of 26.4 g hardener was added to 100 g resin in a 1200 mL metal beaker. For a 400 g batch, that is 316.46 g resin and 83.54 g hardener. The beaker was placed under a Ross High Shear Mixer (HSM-100 LSKI) with 2 in. dispersion blade, and the blade was adjusted so that it was centered and close to the bottom of the beaker. The resin and hardener were mixed at 1000 rpm for 3 min, until the two parts were thoroughly mixed. 75 ml of ethyl acetate was added to the mixture, which was then mixed for 3 min at 1500 rpm. Solvent dilution was required to meet a 60 percent fiber volume target for the prepreg material. The

resin/hardener/ethyl acetate mixture was poured into the lined reservoir on the prepregger (Research Tool Corporation Model 40 Hot-Melt Prepregger) for use with AS4 3K Hexcel Hextow continuous carbon fiber. The drum speed used was 160 (1.7 rpm), and the carriage speed was adjusted to minimize tow overlap or gaps. Once the prepreg sheet was 12 in. wide, the prepregger was stopped, a protective sheet of wax paper was laid over the top of the prepreg, and it was cut. The 6×1 ft sheet of prepreg was removed from the drum and cut into 1×1 ft sheets of prepreg, then stored in the freezer at –7 °F.

7.2.2 CF/GNP/Epoxy

For the 2 and 4 wt% Graphene nanoplatelets (GNP) in epoxy and carbon fiber, the GNP were first dispersed in the resin. GNP were to the 1200 ml metal beaker. Amounts are listed below:

- 2 wt% GNP: 8.00 g GNP, 310.13 g resin, and 81.87 g hardener (hardener added later)
- 4 wt% GNP: 16.00 g GNP, 303.80 g resin, and 80.20 g hardener (hardener added later)

Once the GNP was added to the resin, it was mixed by hand to wet all the GNP and prevent dust and loss of material. The beaker containing resin and GNP was placed under a Ross High Shear Mixer, and the blade was adjusted so that it was centered and close to the bottom of the beaker. The resin and GNP were mixed at 3000 rpm for 1 hr. The beaker was moved to the sonicator (Branson 2510) and sonicated for 1 hr at the sonicator's frequency of 40 Hz. After sonication, the hardener was added, and the mixture was mixed in the Ross mixer at 1000 rpm for 3 min. 75 ml of ethyl acetate was added to the mixture, which was then mixed for 3 min at 1500 rpm. The GNP/resin/hardener/ethyl acetate mixture was poured into the lined reservoir on the prepregger, and processed the same way as the carbon fiber/neat epoxy (description in Section 7.2.1).

The prepreg tape was cut to fabricate both $[0]_{12}$ and $[+45, -45]_{3s}$ panels and hand-laid on an aluminum tool for autoclave cure. Nonporous teflon was placed on the tool, followed by stacked prepreg tape. Cork tape was placed around the laminate to limit resin flow. Nonporous teflon was placed on the laminate stack, followed by a 1/8 thick aluminum caul plate. Breather cloth was placed over the caul plate, followed by a vacuum bag. The panels were cured in an autoclave using the following cure cycle: Ramp to 250 °F at 5 °F per minute, hold at 250 °F for 2 hr, ramp to 350 °F at 5 °F per minute, and hold for 2 hr. Finally, the panels were cooled to room temperature. During the ramp to 350 °F, the pressure was increased from 0 to 85 psi. Vacuum was held throughout the cure cycle. Neat epoxy and GNP/epoxy composites without carbon fiber were previously fabricated as described elsewhere (Ref. 38).

7.3 Specimen Testing

7.3.1 Mechanical Testing

Panels were machined into bars for tensile testing using a water jet cutter. Uniaxial bars (tested at 0° and 90°) were cut to 6×0.5 in. (150×13 mm), with 0.75 in. (19 mm) tabs on both sides. ±45° bars were cut to 8×1 in. (200×25 mm) with 1.5 in. (38 mm) tabs on both sides. Tabbing material was a commercial epoxy glass. Prior to testing, the samples were conditioned at 23 °C and 50 percent relative humidity for 2 days. The tensile properties were measured according to ASTM D3039 at a crosshead rate of 2 mm/min for the 0° samples and ±45° samples, and crosshead rate 0.5 mm/min for the 90° samples. A Tinius Olsen mechanical testing machine with 30 kip load cell was used. A 2 in. Epsilon axial extensometer and an Epsilon transverse extensometer collected strain values for the uniaxial bars. Strain gages CEA-00-250UT-350 were used to collect strain values for the ±45° bars. The equations laid out in ASTM D3518 were used to calculate shear stress and strain from the data from the ±45° bars. The tensile tests were conducted at room temperature.

7.3.2 Acid Digestion

The void volume and fiber content of each laminate panel was calculated following ASTM D3171-76 (acid digestion) with six samples tested per material. The matrix material was digested in hot sulfuric acid and hydrogen peroxide solutions and the remaining carbon fibers were filtered through a fine mesh screen. The fibers were flushed with water followed by an acetone rinse. The acetone was evaporated overnight in a fume hood and the fibers were then dried in an oven at 100 °C prior to weighing.

7.3.3 Field Emission Scanning Electron Microscope Imaging

Samples of 4 wt% GNP in CF-reinforced epoxy were imaged at relatively high magnifications using field emission scanning electron microscopy (FESEM). The samples were prepared for FESEM by cutting thin strips, approximately 2 mm thick × 2 mm wide × 10 mm long, so that the transverse tensile fracture surface would be observed. The samples were sputtered with a platinum/palladium coating using a Cressington 208HR sputter coater. The thickness of the coating was 2 nm and was measured with an embedded Cressington film thickness monitor. A Hitachi-S-4700 FE-SEM at 2.0 kV accelerating voltage was used to view the tensile fracture surfaces of the composite samples.

8.0 Results

The results of the simulations and the experiments are described in this section. The material optimization procedure is also described, along with the interactions of experimental and modeling tasks.

8.1 Experimental Results

8.1.1 Acid Digestion Results

Following the acid digestion, it was not certain how much GNP was separated from the carbon fibers prior to weighing. Constituent volume and weight fractions were calculated on the assumption that all the GNP was weighed with the carbon fiber. The contribution of the GNP to carbon fiber volume fraction and void fraction was small (2 percent or less). The relative content for each panel is provided in Table 1. It can be readily observed that as the GNP content goes up, the CF content reduces. The overall void content falls between ~1 to 8 percent, and does not appear to be correlated with the CF or GNP content. Voids were not considered at any level within the multiscale modeling effort.

8.1.2 Field Emission Scanning Electron Microscope Imaging Results

Figure 12 illustrates the GNP and CF as it exists in the epoxy matrix. It is not clear from the FESM as to the level of dispersion of the GNP in the composite. Previous studies by Hadden et al. (Ref. 3) supplemented the experimental data with multiscale modeling to estimate the dispersion level. In that work, predictions assuming four layers of GNP were the most accurate. In the current work, variation in the dispersion is not considered at every scale in the analysis.

TABLE 1.—FIBER, GRAPHENE, AND VOID CONTENT AVERAGES FOR EACH PANEL

Material system	Graphene content in Epoxy (wt%)	Measured composite carbon fiber content (vol%) (Mean±Standard Deviation)	Calculated composite graphene content (vol%) (Mean±Standard Deviation)	Measured void content (%) (Mean±Standard Deviation)
AS4-862-W Unidirectional panel 1	0	64.8±2.0	0	7.42±2.98
AS4-862-W Unidirectional panel 2	0	65.4±3.9	0	4.23±3.00
AS4-862-W ±45 panel 1	0	64.8±1.0	0	3.41±1.56
AS4-862-W ±45 panel 2	0	64.1±4.9	0	2.64±1.81
AS4-862-W-C-300-2 Unidirectional panel 1	2	59.3±2.9	0.39±0.02	7.56±3.2
AS4-862-W-C-300-2 ±45 panel 1	2	56.4±2.5	0.50±0.04	1.17±1.77
AS4-862-W-C-300-4 Unidirectional panel 1	4	40.1±4.6	1.29±0.14	4.86±2.52
AS4-862-W-C-300-4 Unidirectional panel 2	4	50.9±3.6	1.03±0.06	5.06±3.29
AS4-862-W-C-300-4 ±45 panel 1	4	50.6±2.3	1.09±0.05	0.95±1.55

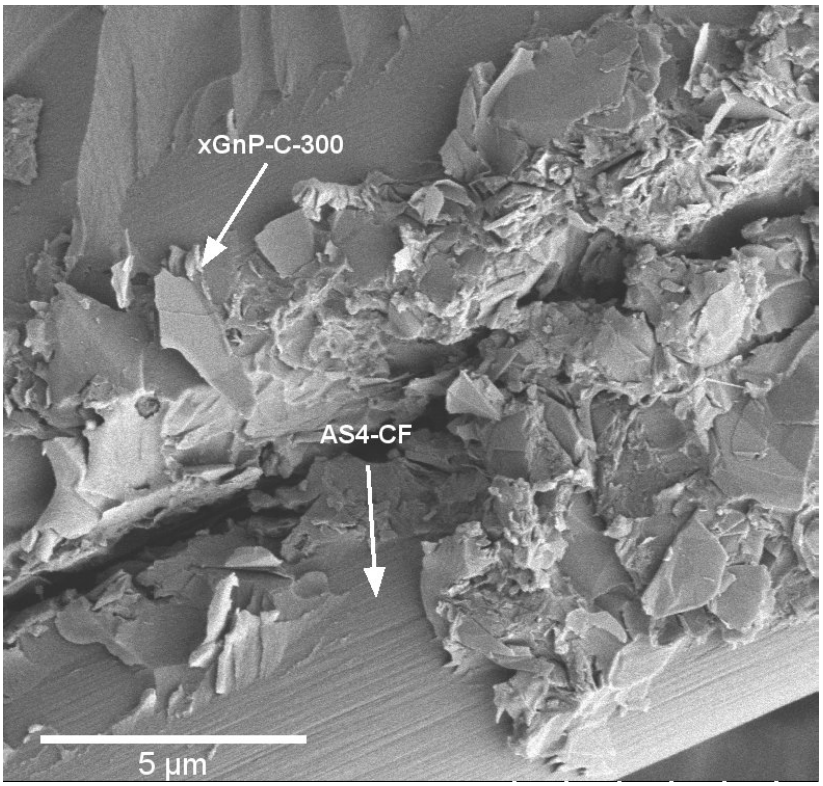

Figure 12.—FESEM image of the fracture surface of a GNP/carbon fiber/ epoxy composite.

8.1.3 Mechanical Testing Results

The longitudinal tensile modulus (Table 2) increased slightly from the baseline panel to the panel with 2 wt% GNP. Both panels with 4 wt% GNP had significantly decreased elastic moduli compared to the baseline and 2 wt% GNP panels. The trends in the longitudinal modulus are primarily a function of the CF content, and the volume fraction of AS4 tended to decrease as GNP was added to the system. The Poisson's ratio increased with increasing GNP content, from 0.30 to 0.39. Values are reported in Table 2 as the mean ±1 standard deviation. Strength values are not reported because, for most bars, the tabs separated before a definite fracture occurred. There were four bars from panel 1 and two bars from panel 2 of the 4 wt% GNP that failed before the tabs separated, and they had an average ultimate strength of 1369±84 MPa and 1510±120 MPa, respectively.

For the transverse samples (Table 3), tensile modulus decreased with increasing GNP content. Again, the volume fraction of CF decreased with increasing GNP content. It is expected, that the transverse modulus would increase with the addition of GNP if the CF volume fraction was consistent across all panels. The baseline panel had the highest transverse tensile modulus of 9.7 GPa, and panel 1 with 4 wt% GNP had the lowest modulus of 6.2 GPa. Strength ranged from 20.7 MPa for panel 1 with 4 wt% GNP to 32.9 MPa for the 2 wt% GNP panel. Poisson's ratios in the transverse direction were not significantly different, and ranged between 0.02 and 0.03. Values are reported in Table 3 as the mean ±1 standard deviation.

The shear modulus (Table 4) decreases from 4.2 GPa for the baseline panel to 3.2 GPa for the panel with 4 wt% GNP. This reduction in shear modulus as a function of the increase in GNP is also attributed to the inconsistent CF volume fractions among the panels. The maximum shear strength of 105 MPa is reached by the panel with 2 wt% GNP. Values are reported in Table 4 as the mean ±1 standard deviation and representative curves can be seen in Figure 13. It appears that the addition of GNP is reducing the shear toughness of the CF/GNP/epoxy system, but this may be a result of the corresponding reduction in CF volume fraction. Therefore, it is assumed that the addition of GNP does increase the shear fracture toughness of the epoxy matrix. The toughening effect resulting from adding GNP to epoxy has been previously demonstrated by Kumar et al. (Ref. 5)

TABLE 2.—LONGITUDINAL TENSILE DATA FOR NEAT, 2 wt%, AND 4 wt% C-300 GRAPHENE IN AS4/862

Formulation	Tensile modulus, E_1 (GPa) (Mean±Standard Deviation)	Major Poisson's ratio, ν_{12} (Mean±Standard Deviation)	Average composite filler content (wt%)	Average composite filler content (vol%)
Baseline AS4/862 panel 1	154.8±4.6 n = 9	0.30±0.03 n = 8	CF- 77.4 GNP- 0	CF- 64.8 GNP- 0
2 wt% GNP in AS4/862 panel 1	158.6±10.2 n = 10	0.32±0.03 n = 10	CF- 72.6 GNP- 0.54	CF- 59.3 GNP- 0.39
4 wt% GNP in AS4/862 panel 1	112.7±12.3 n = 8	0.39±0.06 n = 8	CF- 51.7 GNP- 1.86	CF- 40.1 GNP- 1.29
4 wt% GNP in AS4/862 panel 2	132.6±6.4 n = 9	0.35±0.02 n = 9	CF- 62.9 GNP- 1.43	CF- 50.9 GNP- 1.03

TABLE 3.—TRANSVERSE TENSILE DATA FOR NEAT, 2 wt%, AND 4 wt% C-300 GRAPHENE IN AS4/862

Formulation	Ultimate tensile strength, F_{2t} (MPa) (Mean±Standard Deviation)	Tensile modulus, E_2 (GPa) (Mean±Standard Deviation)	Minor Poisson's ratio, ν_{21} (Mean±Standard Deviation)	Average composite filler content (wt%)	Average composite filler content (vol%)
Baseline AS4/862 panel 2	32.1±3.8 n = 10	9.71±0.40 n = 10	0.031±0.008 n = 8	CF- 75.9 GNP- 0	CF- 65.4 GNP- 0
2 wt% GNP in AS4/862 panel 1	32.9±7.5 n = 9	8.25±0.52 n = 9	0.023±0.004 n = 10	CF- 72.6 GNP- 0.54	CF- 59.3 GNP- 0.39
4 wt% GNP in AS4/862 panel 1	24.7±3.3 n = 7	6.16±0.19 n = 7	0.027±0.003 n = 7	CF- 51.7 GNP- 1.86	CF- 40.1 GNP- 1.29
4 wt% GNP in AS4/862 panel 2	20.7±4.4 n = 9	7.57±0.34 n = 9	0.026±0.005 n = 8	CF- 62.9 GNP- 1.43	CF- 50.9 GNP- 1.03

TABLE 4.—SHEAR DATA FOR NEAT, 2 wt%, AND 4 wt% C-300 GRAPHENE IN AS4/862

Formulation	Ultimate shear strength, F_6 (MPa) (Mean±Standard Deviation)	Shear modulus, G_{12} (GPa) (Mean±Standard Deviation)	Average composite filler content (wt%)	Average composite filler content (vol%)
Baseline AS4/862 panel 1	93.1±10.3 n = 8	4.24±0.19 n = 8	CF- 74.9 GNP- 0	CF- 64.8 GNP- 0
Baseline AS4/862 panel 2	82.1±12.9 n = 8	4.15±0.26 n = 8	CF- 73.6 GNP- 0	CF- 64.1 GNP- 0
2 wt% GNP in AS4/862 panel 1	105.2±2.6 n = 9	3.72±0.17 n = 9	CF- 66.3 GNP- 0.66	CF- 56.4 GNP- 0.50
4 wt% GNP in AS4/862 panel 1	90.8±8.7 n = 9	3.15±0.23 n= 9	CF- 60.6 GNP- 1.5	CF- 50.6 GNP- 1.09

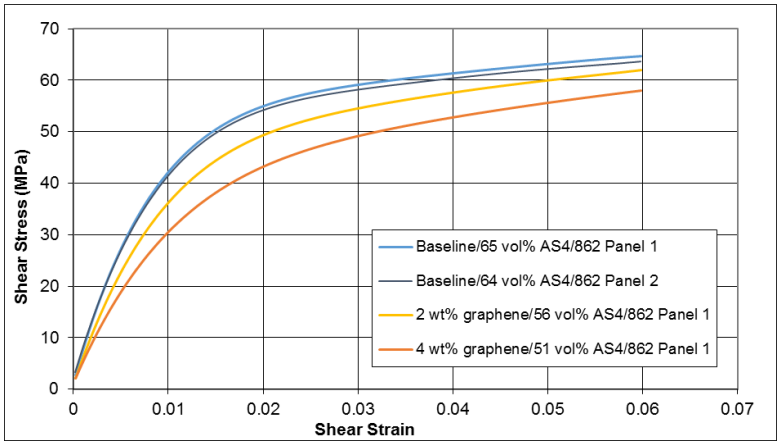

Figure 13.—Average shear stress-strain curves for shear tests up to 0.06 strain. Graphene content is reported as weight percent in epoxy. Carbon fiber content is reported as volume percent in composite.

8.2 Modeling and Simulation Results

A focus of this project is to estimate the potential for improvement in structural performance that can be achieved by designing new materials and structures containing GNP through ICME. The CEUS forward skirt is heavily loaded in compression and compressive failure is a potential concern. A damage tolerant design for the CEUS forward skirt relies on OHC allowables. It has been shown that the addition of GNP significantly improves the fracture toughness of the epoxy resin (Ref. 5). Since OHC failure due to kink band formation is governed by the nonlinear shear stress-shear strain behavior of the composite matrix, it is desirable to improve the shear toughness, and accordingly the fiber microbuckling resistance, of the composite by adding nano-particles such as GNP.

However, manufacturing of a full-scale space structure and certification/qualification of new materials is extremely costly. Thus, simulation tools can be used to predict potential changes material performance affected by changes in processing and manufacturing (such as adding nano-particles) and explore new design concepts. As part of this project, two potential material systems were chosen for the design of the CEUS barrel section: 56 percent (by volume) AS4 CF with EPON862 epoxy (AS4/EPON862) and 56 percent CF with EPON862 containing 1.21 percent volume fraction C-300 GNP dispersed in groups of four layers (AS4/C-300/EPON862). This preliminary work utilized these two material systems to develop a multiscale ICME workflow (Figure 3 and Figure 4) crucial for the implementation of ICME.

TABLE 5.—RELATIVE AS4 AND C-300 GNP VOLUME FRACTIONS, C-300 GNP DISPERSION, INVOLVED MULTISCALE LEVELS, AND PURPOSE OF SIMULATIONS PERFORMED

$v_{CF}^{(2)}$	$v_{GNP}^{(2)}$	$v_{GNP}^{(3)}$	$v_{GNP}^{(5)}$	GNP dispersion	Simulation levels	Purpose
N/A	N/A	0.0121	0.33	4 Layers	5-3	Validation with heritage data (Ref. 30)
0.648	0	0	0	N/A	2	Validation with experimental data
0.564	0.005	0.0115	0.33	4 Layers	5-1	Validation with experimental data
0.56	0	0	0	N/A	5-0	Design of CEUS
0.56	0.0053	0.0121	0.33	4 Layers	5-0	Design of CEUS

The GNP volume fraction in the AS4/C-300/EPON862 system was chosen as a nominal volume fraction that could be attained realistically without any loss in theoretical performance, based on previous work (Refs. 30 and 38). Moreover, the dispersion level of four GNP sheets was selected from previous simulation results that showed that predictions of elastic properties considering this dispersion level matched best with experimental data (Refs. 3 and 30). In addition to the multiscale simulations performed for design of the CEUS, several other analyses were conducted to validate the models against experimental data produced as part of this effort and heritage experimental data (Ref. 30). A summary of all the multiscale simulations that were completed, including relative volume fraction of each phase (P) at every level (L), is given in Table 5. The absolute volume fraction of the GNP within the AS4/C-300/EPON862 composite is calculated for Levels 2 using,

$$v_{GNP}^{(2)} = \left(1 - v_{CF}^{(2)}\right) v_{GNP}^{(3)} \tag{15}$$

The volume fractions of the phases do not change as certain scales are traversed:

$$\begin{gathered} v_{GNP}^{(2)} = v_{GNP}^{(0)} = v_{GNP}^{(1)} \\ v_{GNP}^{(2)} = v_{GNP}^{(0)} = v_{GNP}^{(1)} \\ v_{GNP}^{(3)} = v_{GNP}^{(4)} \end{gathered} \tag{16}$$

Simulation results from each scale are presented in each of the following subsections in hierarchical order (from the lowest to highest scale) according to Figure 2.

8.2.1 Level 5: Molecular Dynamics Modeling of C-300/EPON862—Linear Elastic Results

Table 6 lists the elastic properties for the C-300 GNP and EPON862 MD RUCs with 80 percent crosslink densities and four levels of dispersion (1-4 layers) of the epoxy matrix obtained in Hadden et al. (Ref. 3) The through-thickness stiffness properties E_z, G_{xz}, G_{yz}, associated with the *z-direction*, are incredibly low relative to the other stiffness values. This because the GNP sheets are only bonded to the surrounding epoxy and each other through Van der Waals forces which offer very little resistance to displacement in the *z*-direction. The E_x and E_y values are nearly identical due to material symmetry. The quality of GNP dispersion is considered to decline as the number of GNP layers is increased. Yet, the stiffness properties increase. The final volume of the simulation box does not change as GNP layers are added. So, the inclusion of additional layers results in an RUC with increased GNP volume fraction which yields higher stiffness values even though the dispersion is considered poor. Following the multiscale hierarchy (Figure 2) and multiscale modeling workflows (Figure 3 and Figure 4). These elastic properties were used as input in the Level 4 micromechanics model.

TABLE 6.—PREDICTED ELASTIC PROPERTIES OF C-300/EPON862 RUC FROM MD SIMULATIONS (MODULI GIVEN IN GPA)

GNP layers	GNP volume fraction	E_x	E_y	E_z	G_{xy}	G_{xz}	G_{yz}	V_{xy}	V_{xz}	V_{yz}	V_{yx}	V_{zx}	V_{zy}
1	0.111	93.4	94.8	2.432	0.243	0.001	0.001	0.130	0.460	0.471	0.158	0.109	0.025
2	0.187	174.6	172.5	2.731	0.424	0.001	0.001	0.168	0.437	0.524	0.153	0.056	0.015
3	0.271	239.4	238.3	3.005	0.582	0.001	0.001	0.152	0.440	0.446	0.151	0.010	0.034
4	0.330	293.1	295.5	3.251	0.725	0.001	0.001	0.159	0.455	0.452	0.156	0.011	0.009

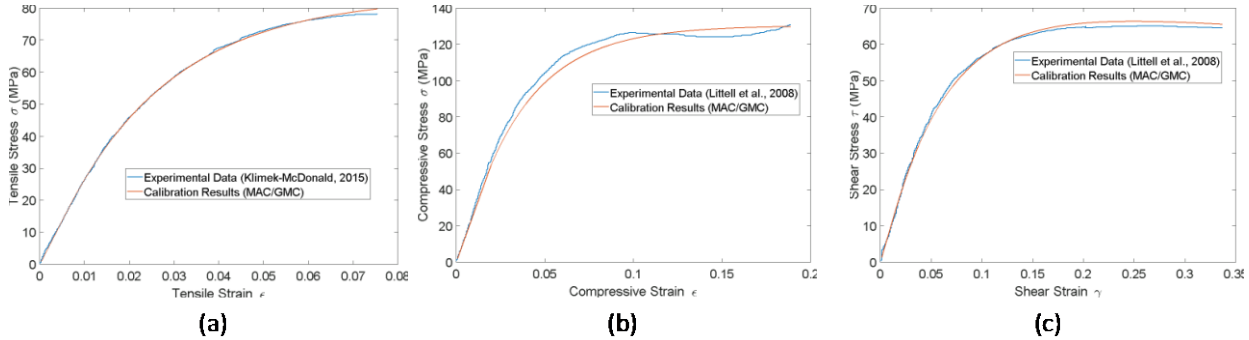

Figure 14.—MAC/GMC calibration of MMCDM parameters for pure EPON862 compared to experimental data. (a) Tension. (b) Compression. (c) Shear.

8.2.2 Level 4: Micromechanics Modeling of C-300/EPON862—Characterization of Nonlinear Mechanical Properties

The MMCDM parameters used to model damage in the EPON862 epoxy system at Level 4 were calibrated against tensile data from Klimek-McDonald (Ref. 30) and compressive and shear data from Littell et al. (Ref. 31). Comparison between the calibrated results, obtained from MAC/GMC, and the experimental data are presented in Figure 14 for tension (Figure 14(a)), compression (Figure 14(b)), and shear (Figure 14(c)). It can be readily observed that the calibration results correlate well with the experimental data. These calibrated MMCDM parameters are then utilized for the matrix subcells (Figure 6) in the Level 4 modeling.

8.2.3 Level 3: Homogenization of Randomly Oriented C-300 in EPON862 Results

At Level 3, the nonlinear response of the Level 4 RUCs are averaged over multiple orientations to obtain an approximation of the nonlinear behavior of an EPON862 RVE, containing randomly oriented C-300 particles, with Equations (6) to (12). These results are shown in Figure 15. The simulations predict significantly higher damage initiation stresses, indicated by the deviation of the stress-strain curves from linearity, than observed in the neat resin, shown in Figure 14. Moreover, the tangent slope of the shear stress-shear strain curve for the C-300/EPON862 (Figure 15(c)) material is higher than for pure EPON862 (Figure 14(c)), illustrating that the numerical method is predicting the addition of GNP will yield a shear toughening effect.

The Level 3 prediction of the nonlinear stress-strain behavior of EPON862 with 1.21 percent volume fraction C-300 is compared to experimental data in Figure 16. Reasonable agreement between the analysis prediction and experimental data was achieved up to 2 percent strain. After 2 percent strain, the analysis predicts a stiffer response than the experiment. This is most likely a facet of the assumption that the subcell containing C-300 and EPON862 at Level 4 is elastic.

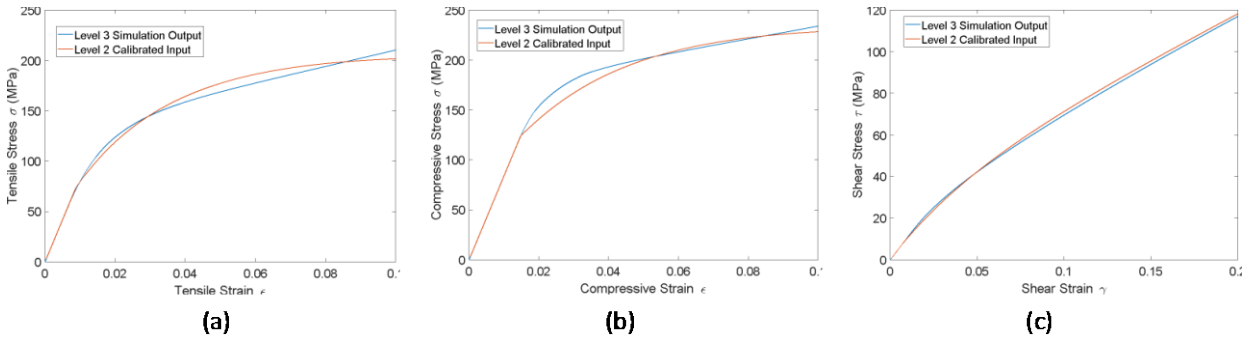

Figure 15.—Results from Level 3 simulation of randomly oriented GNP within EPON862 compared to calibrated MMCDM input for homogenized GNP/EPON862 subcells at Level 2. (a) Tension. (b) Compression. (c) Shear.

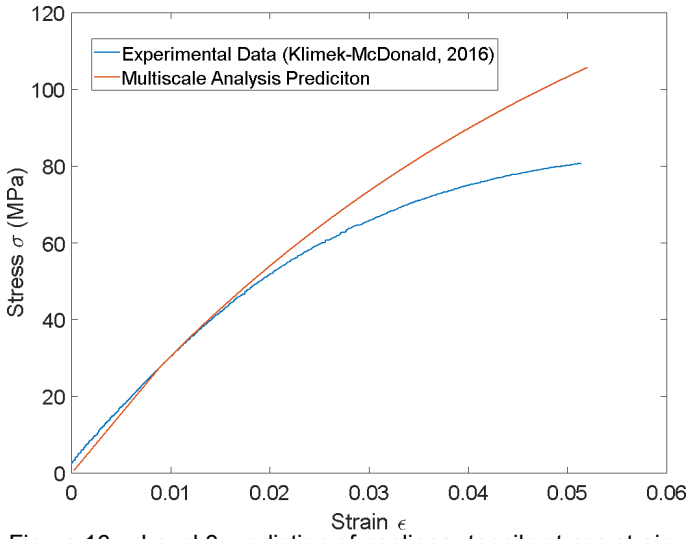

Figure 16.—Level 3 prediction of nonlinear tensile stress strain response of EPON862 epoxy with 1.21 percent volume fraction GNP compared to experimental data.

8.2.4 Level 2: Micromechanics Modeling of AS4/C-300/EPON862

The elastic properties for 56 percent AS4/ 1.21 percent C-300/EPON862 predicted using MAC/GMC and the Level 2 RUC (Figure 7) are given in Table 7. These elastic properties are utilized at Levels 1 and 0 and are assumed to be transversely isotropic. Additionally, the stress strain results obtained from Level 3 are used to calibrate MMCDM inputs for subcells within the Level 2 RUC that represent the effective response of C-300/EPON862. Again, Figure 15 shows good correlation between the outputs at one scale and then the inputs used at the next highest scale. This micromechanics model is used to predict the nonlinear inputs for the progressive damage theory (ST) used in the FEM model at the next level.

Validation of the multiscale analysis work flow is achieved at Level 2 by modeling the AS4/EPON862 and AS4/C-300/EPON862 systems under an applied shear strain and comparing with the experimental data presented in Section 8.1.3. Figure 17 shows very good agreement between the prediction and the experimental data for the AS4/EPON862 system with 64.8 percent AS4 volume fraction. The prediction of the AS4/C-300/EPON862 system (Figure 18) with 56 percent AS4 volume fraction and 1.15 percent GNP volume fraction exhibits significant error in the stiffness and the nonlinear evolution. The lower initial stiffness predicted from the analysis indicates that the employed GNP dispersion level of four layers may be inaccurate, and the GNP may be more well dispersed in the epoxy. As with the error attributed in Figure 16, the error in the nonlinear portion of the stress-strain curve may

be a result of the linear treatment of the GNP/epoxy subcell at Level 4. Furthermore, it may be that the calibration of the MMCDM parameters for the composites containing GNP was performed at a less than ideal scale. This is because the addition of GNP may change the evolution of damage and/or the damage mechanisms themselves. Thus, it might be more accurate to calibrate the MMCDM parameters for the homogenized C-300/EPON862 subcells against C-300/EPON862 experimental data. Further investigation must be conducted to assuredly ascertain the source of error.

TABLE 7.—PREDICTED ELASTIC PROPERTIES FOR AS4/EPON862 AND AS4/C-300/EPON862 USED IN DESIGN OF CEUS

System	$v_{CF}^{(2)}$	$v_{GNP}^{(3)}$	E_{11} (GPa)	E_{22} (GPa)	ν_{12}	G_{12} (GPa)
AS4/EPON862	0.56	0	130.6	6.2	0.36	3.1
AS4/C-300/EPON862	0.56	0.0121	130.7	6.6	0.36	3.6

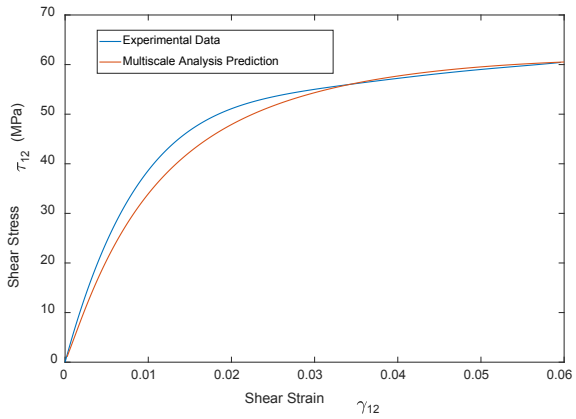

Figure 17.—Level 2 prediction of nonlinear shear stress-strain response of AS4/EPON862 with 64.8 percent AS4 volume fraction compared to experimental data.

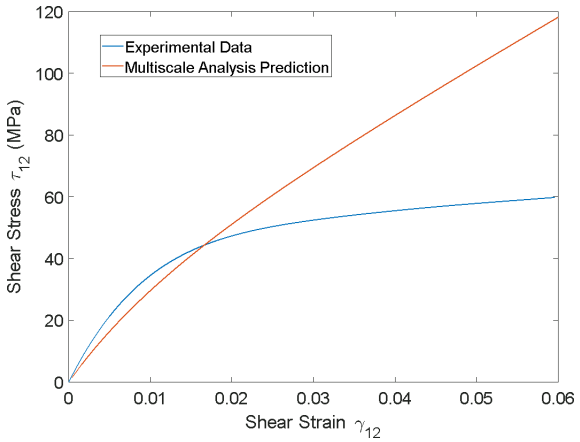

Figure 18.—Level 2 prediction of nonlinear shear stress-strain response of AS4/GNP/EPON862 with 56 percent AS4 volume fraction and 1.15 percent GNP volume fraction in the EPON862 matrix.

8.2.5 Level 1: Finite Element Modeling Results for Open Hole Compression of AS4/C-300/EPON862 Laminates

Simulations of both the pure EPON862 and C-300/EPON862 systems are used within the Level 2 RUC (Figure 7) to predict the matrix microdamage function ST inputs, which are used at Level 1 for the AS4/EPON862 and AS4/C-300/EPON862 systems. The Level 2 MAC/GMC simulation outputs and Level 1 calibrated ST inputs are shown in Figure 19 for the AS4/EPON862 system under transverse tension, transverse compression, and shear and for AS4/C-300/EPON862 in Figure 20. Figure 21 shows the toughening effect of the addition of GNP under transverse tension, compression, and shear.

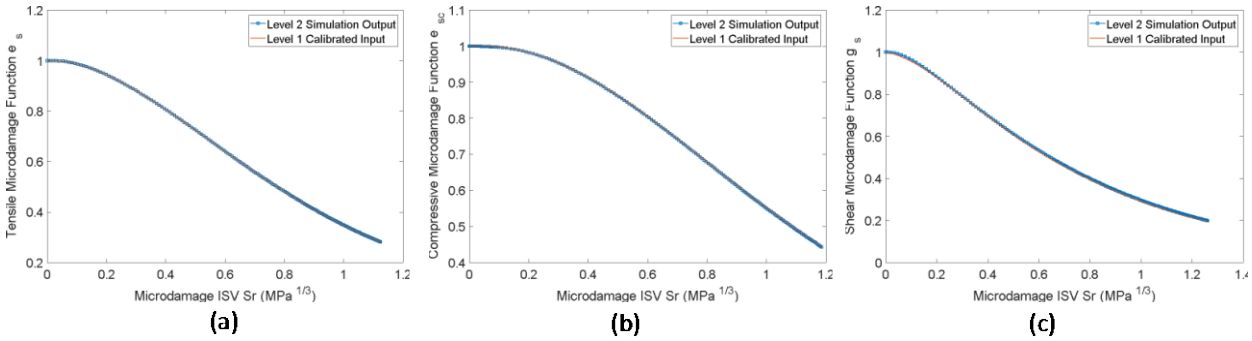

Figure 19.—Normalized stiffness versus dissipated energy potential (microdamage ISV) calculated from Level 2 simulation of AS4/EPON862 composite lamina compared to microdamage function input for Level 1 FEM/ST simulation of OHC of AS4/EPON862 cross-ply laminate. (a) Transverse tension. (b) Transverse compresson. (c) Shear.

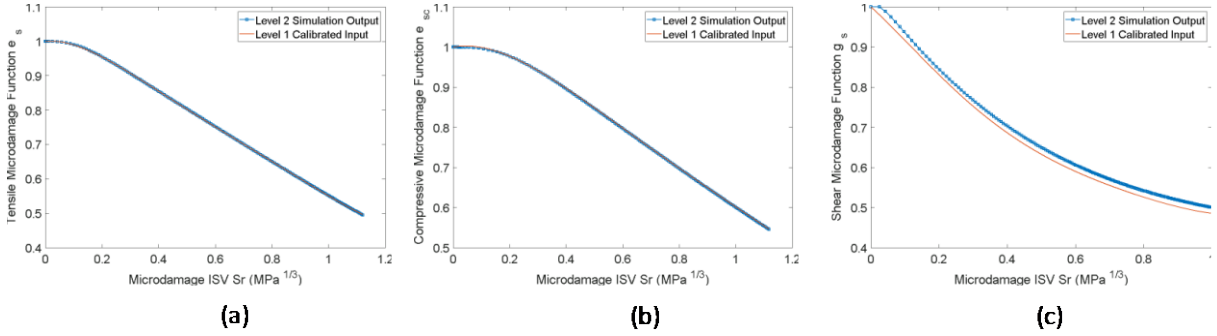

Figure 20.—Normalized stiffness versus dissipated energy potential (microdamage ISV) calculated from Level 2 simulation of AS4/C-300/EPON862 composite lamina compared to microdamage function input for Level 1 FEM/ST simulation of OHC of AS4/C-300/EPON862 cross-ply laminate. (a) Transverse tension. (b) Transverse compresson. (c) Shear.

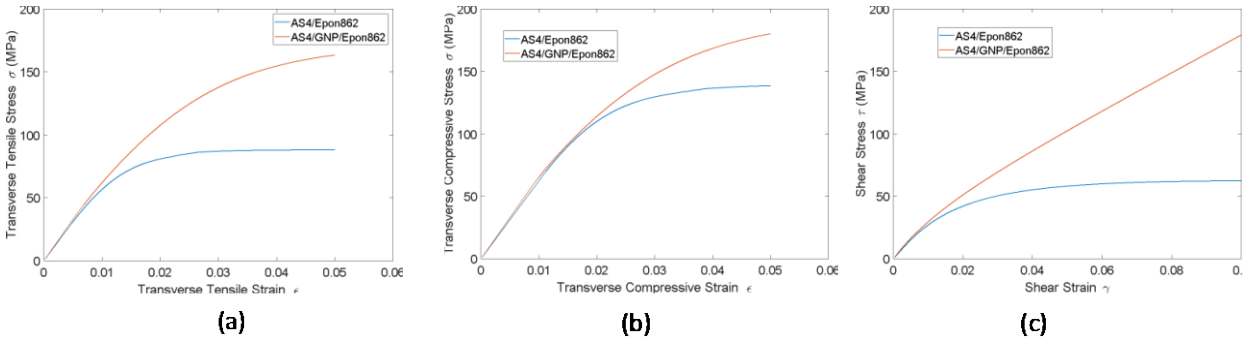

Figure 21.—Comparison of stress-strain response of AS4/EPON862 composite ply with 56 percent volume fraction of AS4 and AS4/GNP/EPON862 composite ply with 56 percent volume fraction of AS4 and 1.21 percent volume fraction of GNP within EPON862 matrix. (a) Transverse tension. (b) Transverse compression. (c) Shear.

The two sets of microdamage functions for AS4/EPON862 and AS4/GNP/EPON862 given in Figure 19 and Figure 20, respectively, are used to model matrix microdamage with NEST in the OHC specimens and predict the OHC strengths. The OHC allowables used for the design of the CEUS structure (Level 0) are calculated from the OHC ply failure stresses.

Figure 22 shows the far field stress versus average strain in the OHC specimen gage section for the two systems. The system containing the nanoparticles exhibited a significantly tougher response than the system with the pure epoxy. Moreover, the AS4/C-300/EPON862 composite displayed a strain-hardening behavior with damage evolution, whereas the AS4/EPON862 composite softened globally.

The ply failure stresses given in Table 8 were calculated when the tangent slope of the stress-strain curve in Figure 22 decreased more than 80 percent from its original value. Once the change in the tangent slope exceeded this threshold, the strains in the 0° ply of an element far from the notch where there is no damage and the strain fields are homogenous, was noted. The strains were then multiplied by the corresponding elastic modulus, given in Table 7 to arrive at the failure stresses in Table 8.

Figure 23 shows the deformation of the gage section and the angular orientation of the fibers (SDV1), relative to the original fiber direction, in each OHC specimen when it was deemed that it has failed according to the criterion described above. The contour limits of the fiber rotation were set to ±5°. The formation of a kink band can clearly be observed in both the AS4/EPON862 and the AS4/C-300/EPON862 specimens, validating that the correct failure mechanism was predicted by the model. Moreover, the kink band in the AS4/C-300/EPON862 specimen was wider. This indicates that more energy was dissipated during the kink band formation, a result of the increased toughness of the matrix, due to the presence of GNP.

Figure 24 and Figure 25 show the progression of the ST microdamage ISV *Sr* (SDV2) in the AS4/EPON862 and AS4/C-300/EPON862 specimens, respectively. In both specimens, fiber microbuckling is precluded by matrix shear splitting, a less severe damage mechanism. While the specimens are damaged due to shear splitting the global stress-strain response remains nearly linear. However, as the matrix damage starts to promote fiber kinking, the stress-strain curve begins to exhibit some nonlinearity. Finally, the kink band formation supersedes the shear splitting, and the specimen is no longer capable of supporting significant increases in the applied load. A comparison of Figure 24 and Figure 25 shows that the splitting damage in the AS4/C-300/EPON862 specimen is more diffuse and lower in magnitude, supporting the hypothesis that the addition of GNP increases the shear toughness of the system.

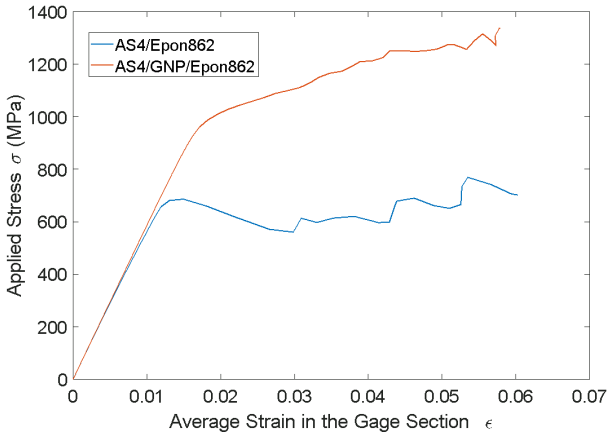

Figure 22.—Applied compressive stress versus average compressive strain in gage section of OHC cross-ply specimen for AS4/EPON862 system with 56 percent volume fraction of AS4 and AS4/C-300/EPON862 system with 56 percent volume fraction of AS4 and 1.21 percent volume fraction of GNP within EPON862 matrix.

TABLE 8.—PREDICTED OHC PLY FAILURE STRESSES

System	$v_{CF}^{(2)}$	$v_{GNP}^{(3)}$	X_σ (MPa)	Y_σ (MPa)	Z_σ (MPa)
AS4/EPON862	0.56	0	1257	60.4	30.7
AS4/C-300/EPON862	0.56	0.0121	1831	92.4	50.9

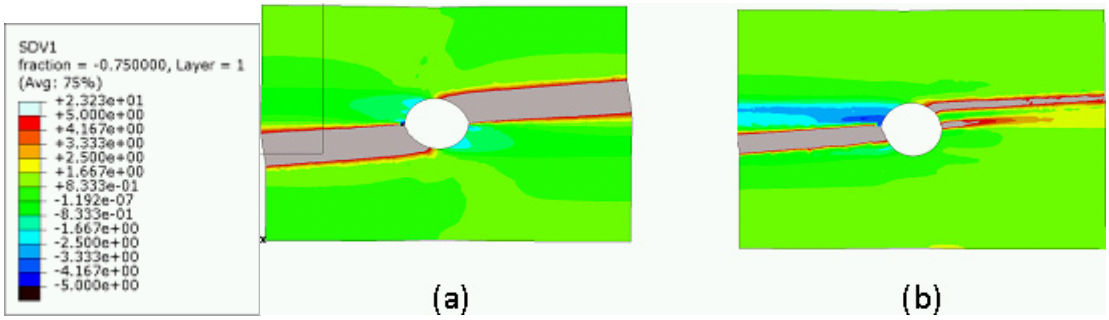

Figure 23.—Failure of OHC cross-ply specimen due to kink band formation. (a) AS4/EPON862 system with 56 percent volume fraction of AS4. (b) AS4/C-300/EPON862 system with 56 percent volume fraction of AS4 and 1.21 percent volume fraction of GNP within EPON862 matrix.

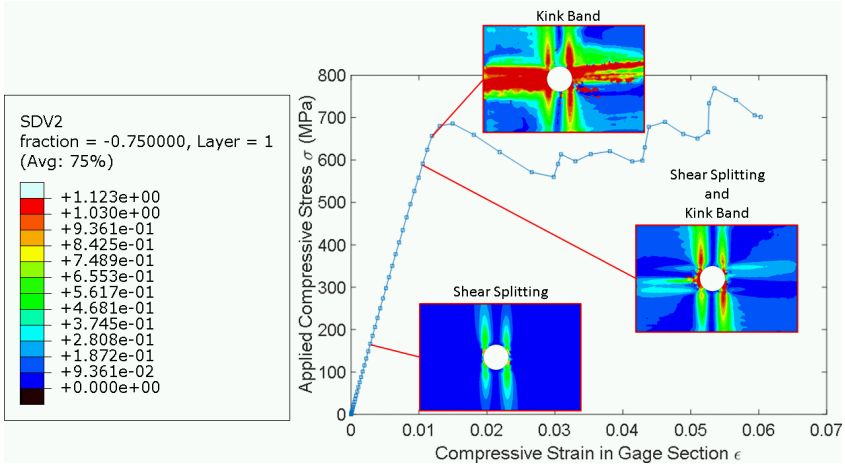

Figure 24.—Damage progression predicted with ST in OHC cross-ply specimen composed of AS4/EPON862 system with 56 percent volume fraction of AS4.

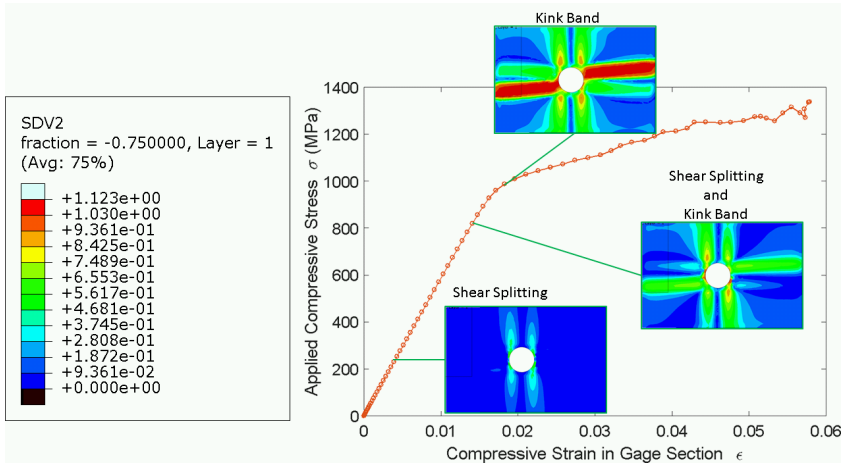

Figure 25.—Damage progression predicted with ST in OHC cross-ply specimen composed of AS4/C-300/EPON862 system with 56 percent volume fraction of AS4 and 1.21 percent volume fraction of C-300 within EPON862 matrix.

8.2.6 Coefficient of Linear Thermal Expansion Results

The calculated CLTEs are shown in Table 9. They were determined by averaging the results from the heating and cooling methods. The in-plane CLTEs (x and y directions in Figure 5) were all negative values meaning that the in-plane dimension of box shrank at the higher temperature in those directions. The elastic properties used in Equation (14) were taken from Table 6, and the randomized CLTE values are given in Table 9.

Subsequent to randomization, the CLTE of the C-300/EPON862 system is calculated by homogenizing a 2×2×2 RUC with MAC/GMC to account for the appropriate volume fraction of C-300. The volume fraction of the (inclusion) subcell which utilized the C-300/EPON862 CLTEs predicted using MD was calculated for overall GNP volume fractions ranging from 0 to 5 percent with 0.5 percent increments and different dispersion levels. These results are given in Table 10.

Table 11 shows the CLTEs predicted for a unidirectional AS4/C-300/EPON862 lamina calculated using MAC/GMC and the RUC presented in Figure 7. The matrix subcells (red) are assumed to have CLTE properties representative of homogenized C-300/EPON862. The CLTEs for 1.21 percent GNP volume fraction in the matrix is obtained through linear interpolation.

TABLE 9.—PREDICTED CLTES OF C-300/EPON862 FROM MD SIMULATIONS

GNP layers	αx [ppm/°C]	αy [ppm/°C]	αz [ppm/°C]	αr [ppm/°C]
1	–7.34	–9.34	260.02	9.95
2	–7.25	–8.31	234.41	1.69
3	–7.94	–6.48	210.94	–1.53

TABLE 10.—PREDICTED CLTES OF C-300/EPON862 FROM MAC/GMC

GNP volume fraction	α_r[ppm/°C]			
	1 layer	2 layers	3 layers	4 layers
0.000	86.00	86.00	86.00	86.00
0.005	82.39	83.64	84.32	84.58
0.010	78.69	81.22	82.59	83.11
0.015	74.97	78.78	80.86	81.64
0.020	71.25	76.33	79.10	80.15
0.025	67.53	73.87	77.35	78.67
0.030	63.85	71.40	75.58	77.17
0.035	60.19	68.95	73.82	75.67
0.040	56.57	66.50	72.05	74.17
0.045	52.98	64.06	70.29	72.67
0.050	49.44	61.63	68.53	71.16

TABLE 11.—PREDICTED CTES FOR AS4/EPON862 AND AS4/C-300/EPON862 USED IN DESIGN OF CEUS

System	$v_{CF}^{(2)}$	$v_{GNP}^{(3)}$	α_1 (10^{-6}/°C)	α_2 (10^{-6}/°C)
AS4/EPON862	0.56	0	0.038	59.25
AS4/C-300/EPON862	0.56	0.0121	0.053	57.08

8.3 Determination of Stress Allowables

Because the structural application of this study is a compression-dominated launch vehicle structure, emphasis has been placed on the impact of GNP on ply-level OHC stress allowables. However, to complete the sizing process for the structure, tensile stress allowables are needed as well. These tensile stress allowables were taken as average ultimate tensile stresses of the baseline AS4/EPON862 (neat EPON862 matrix) panel specimens tested in longitudinal and transvse tension. To isolate the impact of the GNP on the OHC allowables, no enhancement of these tensile allowables from GNP was considered. Rather, identical tensile allowables were employed for the composite, both with and without GNP reinforced matrix. These values are shown in Table 12, where Ftu1 and Ftu2 are the longitudinal and transverse tensile allowables, Fcu1 and Fcu2 are the longitudinal and transverse compressive allowables, and Fsu is the shear allowable.

To determine the OHC allowables (for longitudinal and transverse compression, as well as in-plane shear), the cross-ply open hole compression progressive failure simulation results, discussed above, were used. The predicted far-field in-plane shear failure stresses for the neat EPON862 matrix composite and the composite with 1.21 vol% C-300 GNP in the matrix are 30.7 and 50.9 MPa, respectively. These are reasonable values, given the average test ultimate shear strength data for the unnotched composite (82.1 and 93.1 MPa for neat matrix, 105.2 MPa for 2 wt% GNP enhanced matrix). As such, these predictions were used as the OHC shear allowables (Table 12).

The predicted far-field compressive stresses in the longitudinal and transverse directions are quite high (1257 and 60.4 MPa for neat matrix, 1831 and 92.4 MPa for GNP enhanced matrix). To arrive at more realistic longitudinal and transverse OHC allowables, these values were scaled based on a similar material system, with well-established pristine and damage tolerant allowables, AS4/3502, whose properties are available in MIL-HDBK-17-2E (Ref. 39). The assumption was made that the ratio of the pristine longitudinal tensile allowable (Ftu1) to the damage tolerant longitudinal compressive allowable (Fcu1-DT) is the same between the reference AS4/3502 and current AS4/EPON862 material systems. For AS4/3502, (Fcu1-DT)/(Ftu1) = (519 MPa/1413 MPa) = 0.367. Then, given that for AS4/EPON862, Ftu1 = 1369 MPa, we have (Fcu1-DT) = (0.367)(1369 MPa) = 503 MPa, which represents a ratio of (503 MPa/1257 MPa) = 0.400 vs. the predicted OHC longitudinal failure stress. This ratio was used to scale, or knock-down, the predicted longitudinal and transverse OHC ply failure stresses to arrive at the employed allowables, which are given in Table 12. These values are reasonable and conservative with respect to the established neat AS4/3502 material system damage tolerant allowables (Ref. 39). Note also that they maintain the predicted ratio between the OHC failure stresses for the composite with neat matrix vs. that with GNP enhanced matrix. This procedure of scaling the predicted strengths using established allowables to arrive at more reasonable predicted allowables demonstrates the use of engineering decision making within the ICME workflow to assuage error and uncertainty introduced at some level within the multiscale modeling. Techniques such as this may be necessary when implementing an ICME framework because the predictive capability of state-of-the-art multiscale progressive failure tools has not completely matured (Ref. 40).

TABLE 12.—PLY-LEVEL STRESS ALLOWABLES EMPLOYED FOR THE AS4/EPON862 MATERIAL SYSTEM WITH 56 vol% CF

Allowable	AS4/EPON862	AS4/1.21 vol% C-300/EPON862
Ftu1 (MPa)	1369	1369
Ftu2 (MPa)	32.1	32.1
Fcu1 (MPa)	503	733
Fcu2 (MPa)	24.2	37.0
Fsu (MPa)	30.7	50.9

8.4 Sizing Results

The sizing process for the CEUS forward skirt was completed using the HyperSizer Structural Sizing Software (Ref. 34), along with the MSC/NASTRAN finite element solver (Ref. 35). Two separate designs were considered, one based on the 56 vol% AS4/EPON862 material system and the other based on the 56 vol% AS4/1.21 vol% C-300/EPON862 material system, in order to evaluate the mass savings associated with the GNP enhanced matrix. The CEUS forward skirt composite panels were designed as aluminum honeycomb core sandwich panels, with composite laminate facesheets. The finite element model, simulated load introduction structure, load cases, and relevant factors were discussed previously in Section VI.D. Four aluminum honeycomb core candidate materials were considered in the sizing, Hexcel (3.1 pcf ⅛-5052-0.0007, 3.1 pcf ⅜-5052-0.002, 4.5 pcf ⅛-5052-0.0010, and 6.1 pcf ⅛-5052-0.0015) (Ref. 41). The sizing consistently chose the two lightest core materials, and for the design presented herein, the core was eventually fixed as 3.1 pcf ⅛-5052-0.0007 material, which is commonly used by NASA, in order to improve the design manufacturability. The core thickness was sized between a minimum of 0.75 in. (19 mm) and a maximum of 2 in. (51 mm). The sizing produced core thicknesses of 1 to 1.5 in. (25 to 38 mm), and for manufacturability, the core thickness was eventually fixed at 1 in. (25 mm).

The honeycomb sandwich panel facesheets were kept symmetric and balanced, and the top and bottom facesheets were kept the same, with the exception of the acreage splice build ups (Figure 10). These facesheets are intended to represent a bonded splice between the two acreage panels, and thus the top facesheet has a splice layup on top of the acreage layup, whereas the bottom facesheet has the mirrored splice layup added to the bottom of the facesheet. In this way, these acreage splice build up panels remain symmetric overall. Note also that, the densities of the plies are set to the theoretical values based on their constituent densities and volume fractions (1.5304 g/cc for the neat matrix system and 1.5347 g/cc for the GNP enhanced resin system), while a ply thickness of 0.0875 mm was employed for both systems, which represents a typical value from the tested panels.

The sizing process involved starting with HyperSizer's "Effective Laminates," which are averaged representations of actual laminates based on ply percentages. This allows the sizing process to approach the needed laminate thicknesses. Then HyperSizer automatically generates "Discrete Laminates," which are full ply by ply representations of the composite facesheets, with candidate layups in the neighborhood of the Effective Laminates thickness and ply percentages. Note that, as is common practice at NASA, only 0°, 90°, and ±45° plies were considered for the facesheet designs. After sizing with Discrete Laminates, the panel designs can be sequenced to ensure compatibility between adjacent panel facesheets.

At all stages of the sizing process, as the panel designs evolve, it is critical to iterate the finite element solution for the structure. This allows the load path to change as the relative stiffnesses of the panels are changing. HyperSizer automatically writes new panel definitions in the finite element model to represent the updated design. The software also includes a convenient interface to automatically execute the updated finite element model, and then automatically updates the loads for the next sizing iteration. On the order of 30 finite element/sizing iterations were performed for each of the neat and GNP enhanced designs during the sizing process.

The final designs on the CEUS using the neat EPON862 matrix material system and the GNP enhanced matrix material system are summarized in Table 13. Clearly, the improvement in the predicted OHC allowables offered by the GNP enhancement of the EPON862 matrix has had a considerable impact on the CEUS forward skirt mass. The mass savings for the composite panels is 22 percent, which is mainly attributable to the acreage panel facesheets, which are 24 plies in the case of the neat matrix system and 18 plies for the GNP enhanced matrix system. Note that in both designs, the panels denoted as forward build-up did not require any actual build-up as the acreage panel design was sufficient. The aft build-up panel facesheets did require an additional 12 plies in both cases due to the higher load levels, partly from the thermal loads (Figure 11). Finally, the splice doubler, which was restricted to (45°/–45°) ply pairs in order to minimize concentrating additional load to these splice regions, was also able to half in thickness due to the presence of the GNP enhanced matrix. Recall that the panel designs in the splice doubler region were required to simply add these (45°/–45°) ply pairs to the top and bottom of the

facesheets (while keeping the panel design symmetric). Note that in practice, these splice doublers might be constructed of fabric (rather than tape) plies, oriented at ±45°.

The final margins of safety for the designs, both with and without GNP enhanced matrix, are shown in Figure 26. Both designs are closed, passing all failure checks for all load cases for all panels (any failure would result in a negative margin of safety). Note that, based on the raw sizing, both designs had panels very close to zero margin of safety (indicating a highly optimized design). However, when the changes were made to enable consistent transitions between panels for manufactuability, the margins rise slightly.

Figure 27 shows the controlling failure analysis (the failure check that resulted in the lowest margin of safety) for the two CEUS designs. Recall that, even though the panels are grouped and linked to require the same design, each panel has distinct loading, and thus will have its own controlling criterion. Both designs are controlled by ply level composite strength failure criteria, which explains the importance of the OHC allowables that were used in the sizing. The flatwise tension with interlaminar shear interaction criterion, which represents the tendency of the through-thickness stresses to increase when a curved panel is subjected to bending moments, is also controlling in some locations. Interestingly, the Tsai-Wu criterion is most prevalent in the neat resin matrix design, whereas, in the case of the GNP enhanced resin, the Tsai-Hahn criterion is most prevalent. This difference is due to the different allowables between the two material systems, along with the fact that load paths (and thus the multiaxial load states per panel) are distinct due to the unique structural stiffnesses of the two designs.

TABLE 13.—SUMMARY OF THE CEUS FORWARD SKIRT COMPOSITE PANEL DESIGNS FOR THE MATERIAL SYSTEMS WITH AND WITHOUT GNP ENHANCED MATRIX

	AS4/EPON862	AS4/1.21 vol% C-300/EPON862
Mass	680 lbm (308 kg)	529 lbm (240 kg)
Acreage facesheet	24 plies, (42% 0°, 33% 45°, 25% 90°) $[45°/–45°/0°/0°/0°/45°/90°/90°/0°/0°/–45°/90°]_s$	18 plies, (44% 0°, 44% 45°, 11% 90°) $[45°/–45°/0°/0°/45°/0°/0°/–45°/90°]_s$
Fwd buildup facesheet	24 plies, (42% 0°, 33% 45°, 25% 90°) $[45°/–45°/0°/0°/0°/45°/90°/90°/0°/0°/–45°/90°]_s$	18 plies, (44% 0°, 44% 45°, 11% 90°) $[45°/–45°/0°/0°/45°/0°/0°/–45°/90°]_s$
Aft buildup facesheet	36 plies, (61% 0°, 22% 45°, 17% 90°) $[45°/–45°/0°/0°/0°/0°/45°/0°/90°/90°/0°/0°/0°/0°/$ $–45°/90°/0°/0°]_s$	30 plies, (60% 0, 27% 45, 13% 90) $[45°/–45°/0°/0°/0°/45°/0°/90°/0°/0°/0°$ $/–45°/90°/0°/0°]_s$
Splice doubler	48 plies (100% 45°) Top: $[(45°/–45°)_{24}]$ Bottom: $[(–45°/45°)_{24}]$	24 plies (100% 45°) Top: $[(45°/–45°)_{12}]$ Bottom: $[(–45°/45°)_{12}]$

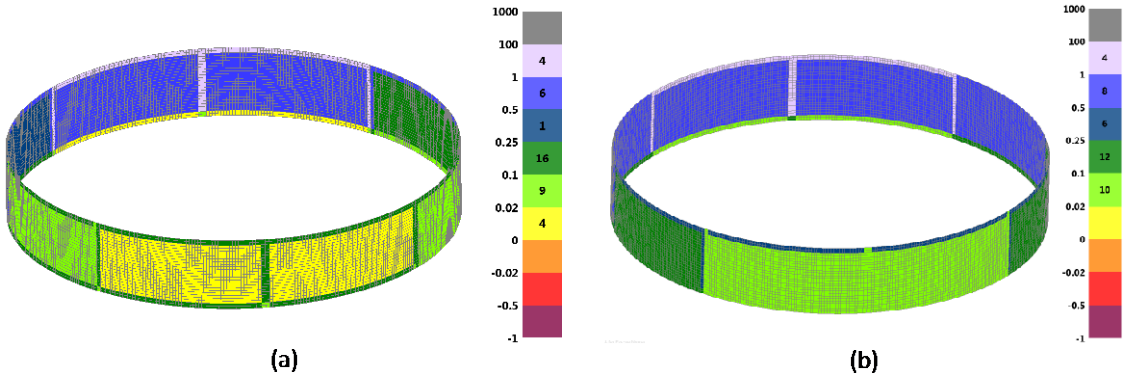

Figure 26.—Margins of safety for the CEUS composite panel designs for (a) the neat epoxy matrix material system and (b) the GNP enhanced matrix system.

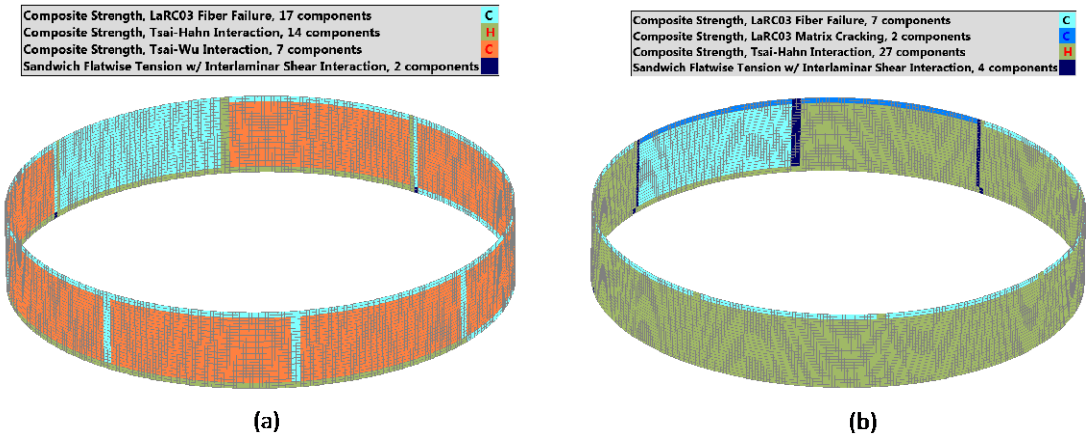

Figure 27.—Controlling failure analysis for the CEUS composite panel designs for (a) the neat epoxy matrix material system and (b) the GNP enhanced matrix system.

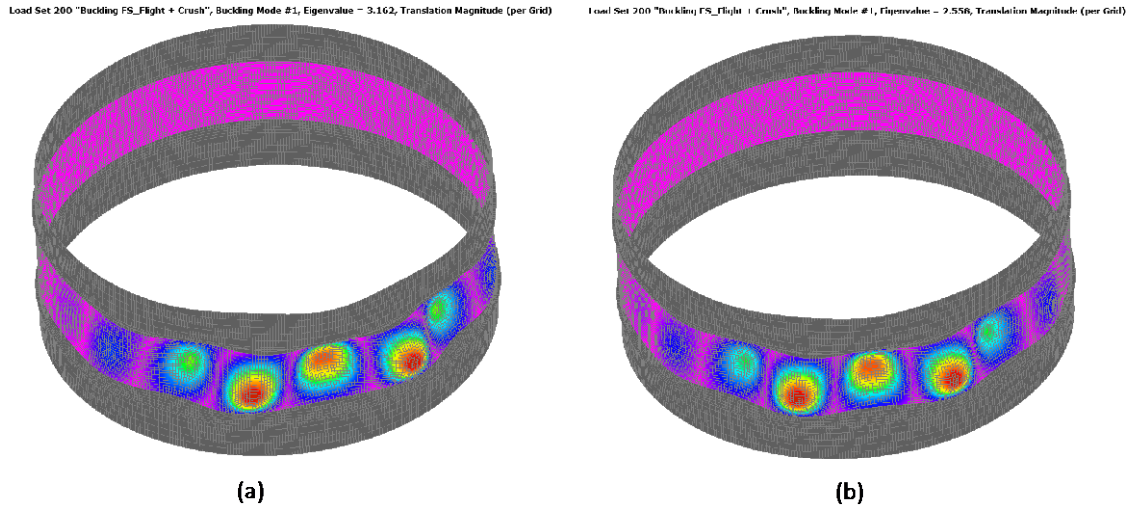

Figure 28.—First buckling mode as predicted by finite element eigenvalue analysis for the CEUS composite panel designs for (a) the neat epoxy matrix material system (eigenvalue = 3.16) and (b) the GNP enhanced matrix system (eigenvalue = 2.56).

As a compressive dominated structure, it is also interesting that panel buckling does not provide the lowest margin of safety for any of the panels. HyperSizer performs a panel buckling check, but this is based on panel level loads, and is only approximate for the entire structure in which all structures (beams and panels) interact. Therefore, it is common practice to perform an independent finite element eigenvalue buckling simulation to ensure that the structure meets global buckling requirements. The standard factor for global buckling includes the 1.4 ultimate factor of safety, along with a buckling knockdown factor of 0.65. Combined, these factors require a global buckling eigenvalue of 1.4/0.65 = 2.15. Global buckling eigenvalue simulations were performed on the final designs for the CEUS forward skirt structure for the material systems without and with GNP enhanced matrix. The resulting buckling mode shapes are shown in Figure 28, along with the eigenvalues (3.16 and 2.56), both of which are above the 2.15 minimum requirement. Note that, in addition to the composite panels, the load introduction structure has been shown in to clarify that it is not buckling. Clearly, the buckling modes are similar between the two designs, with the buckling waves concentrated near the location of highest compression load magnitude. The design using the neat resin system has a somewhat higher eigenvalue. Both designs have some buckling margin, which indicates that a thinner core would probably be acceptable. The resulting thinner panels might then elevate HyperSizer's buckling failure check to be controlling for some panels in Figure 27, but the facesheet designs would still be dictated by the material OHC allowables.

Figure 29 shows the details of the facesheet designs for a one-eighth section of the CEUS forward skirt. Recall that each one-eighth segment can be constructed independently (using readily available autoclaves), and then joined to form the CEUS forward skirt. The top facesheets are shown in Figure 29, but the bottom facesheets are identical, except for the splice panels, whose bottom facesheets are mirrored with respect to the top facesheet (such that the honeycomb sandwich panel remains symmetric). Clearly, both designs are highly manufacturable, with all acreage plies being continuous across the entire one-eighth section. In both cases, transitioning from the aft build up to the acreage requires 12 plies to be dropped from the symmetric layups. The transitions to the longitudinal splice panels, both from the acreage and the aft build ups, require only the addition of the doubler, which in the case of the neat resin system design consists of 24 (45°/–45°) ply pairs, and in the case of the GNP enhanced resin system design consists of 12 (45°/–45°) ply pairs. Recall that longitudinally compliant (45°/–45°) ply pairs are used to avoid adding excess stiffness to the splice, which would tend to cause more load to concentrate in the splice region as the finite element solution is iterated to update the load path.

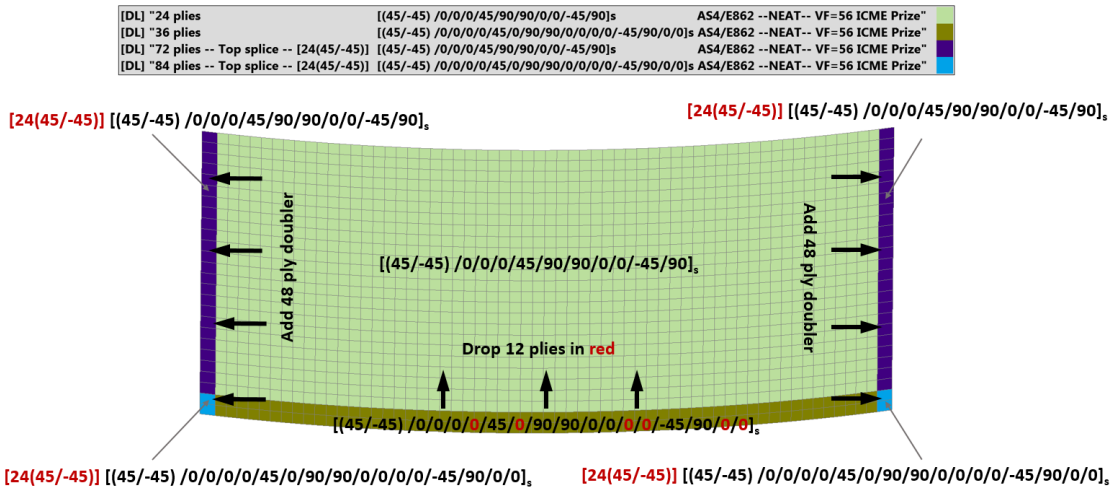

(a)

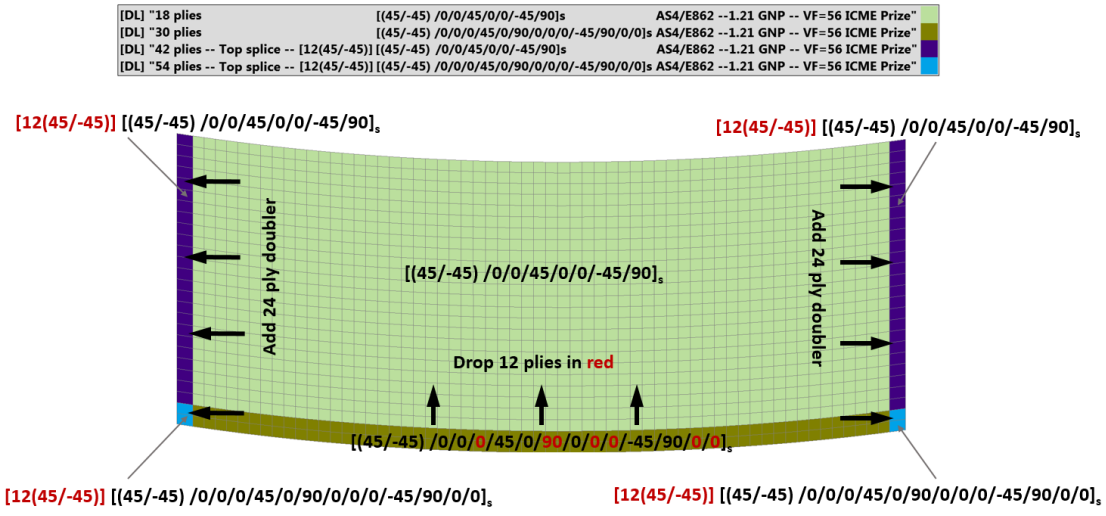

(b)

Figure 29.—Details of the panel top facesheet layups and ply transitions for a one-eighth circumferential section of the CEUS composite panel designs for (a) the neat epoxy matrix material system and (b) the GNP enhanced matrix system.

9.0 Error and Uncertainty Quantification

Uncertainty and error can be introduced at any stage within the ICME workflow, and the error can result from theory, modeling and/or experimentation. Since ICME is to be utilized for rapid, virtual design across multiple scales it is important to understand when (at which scale) error or uncertainty is introduced, the type of error or uncertainty that is introduced, and its effects at the highest (or other pertinent scales), and it must be quantified. In this section various sources of error are identified and quantified. Uncertainty is also identified. However, it is difficult to quantify this uncertainty without a rigorous statistical analysis. As such, the final OHC strengths are scaled based upon reliable data in attempt to reduce the uncertainty in the design.

9.1 Error and Uncertainty in Experiments

Quantification of the uncertainty in the experimental data generated for this project is presented in Section 8.1 in the form of standard deviations. To summarize, there exists ~2 to 11 percent variability in the measured AS4 volume fraction, but ~43 to 151 percent variability in measured void content. Therefore, the uncertainty in the CF content is marginal, but the uncertainty in the void content is substantial. However, the magnitude of the void content is relatively low (~1 to 8 percent), therefore this uncertainty may not be significant. Moreover, voids are not considered in the modeling. The variability in the GNP volume fraction is on the order of that of the CF (~5 to 11 percent). The variability in the longitudinal modulus ranges from ~2 to 11 percent and correlates to the uncertainty in the AS4 volume fraction measurements. Additionally, the variability in the transverse and shear moduli ranges from ~3 to 6 percent and 4 to 7 percent, respectively. The longitudinal strengths exhibited a 6 to 8 percent deviation. Finally, the variation in transverse tensile strength was more pronounced (~12 to 22 percent). Although not enough samples were tested to form a stringent statistical basis, it can be concluded that the experimental data is not an appreciable source of error. Moreover, the uncertainty introduced by this error was minimal because this data was solely used for the purposes of model validation. It was not integrated into the structural design. The longitudinal and transverse strengths for the baseline AS4/EPON862 specimens which ranged from ~6 to 12 percent were used in the design, but they did not contribute to any of the failure criteria that ultimately controlled the design.

9.2 Error and Uncertainty in Multiscale Characterization and Validation

Material characterization occurs at nearly every level within the multiscale modeling framework using a combination of experimental and virtual (simulation) data. This error manifests in the error observed in the multiscale predictions (validation) displayed in Figure 16 to Figure 18, along with contributions from error in the experimental characterization data and numerical modeling techniques and theories. Ultimately, it provides a degree in uncertainty in final performance (mass and margin of safety) calculations. Further data processing is needed to quantify error resulting from characterization and present in the validation. However, effort is taken to assuage this error, and the associated uncertainties, through scaling of the OHC strength to obtain the OHC allowables used in the design, as described in Section 8.3.

9.3 Error and Uncertainty Resulting From Randomization of Nonlinear Mechanical Properties

Because the stiffness evolution implicitly depends on the applied strain and orientation of the unit cell, the averaging integrals from Christensen and Waals (Ref. 19) cannot be solved analytically. Instead, the integrals were converted into summations given in Equations (6) and (7). Although, the error introduced with these approximations cannot be calculated for the entirety of the nonlinear evolution of the stiffness

components of the C-300/EPON862 composite, and estimate of the error can be estimated by comparing the elastic (undamaged) moduli computed using the procedure developed for this work against analytical calculations using the Christensen and Waals (Ref. 19) equations.

Preliminary studies were conducted on a glass fiber/epoxy RUC to determine suitable orientation increments $\Delta\theta$, $\Delta\phi$ to be used in the implementation of the final ICME multiscale modeling workflow. The error in the elastic stiffness components and moduli, as compared to the analytical solutions, are presented in Table 14 for a range of orientation angle increments. This data was used to arrive at an orientation angle incement that provided a fair balance between accuracy and computational efficiency (more MAC/GMC calculations are need to complete the summations as the orientation angle increment is decreased). It was deemed that an increment of 15° provided this balance as it produced less than 10 percent error which is close to the variability observed in the experimental data. Moreover, Figure 30 shows the evolution of C_{33} and C_{23} for the range of $\Delta\theta$, $\Delta\phi$ (delta). It can be seen that the variability in the nonlinear regime of these curves is actually less than that among the elastic values, and the nonlinear results converge somewhere between $\Delta\theta$, $\Delta\phi$ = 15° and 7.5°.

TABLE 14.—ERROR IN ELASTIC STIFFNESS COMPONENTS AND MODULI FROM AVERAGING SUMMATION EQUATIONS (6) TO (10) AS COMPARED TO ANALYTICAL SOLUTION FROM CHRISTENSEN AND WAALS (REF. 19)

$\Delta\theta$, $\Delta\phi$	% Err. in C_{33}	% Err. in C_{23}	% Err. in ν	% Err. in G
45°	9.76	13.8	2.7	4.3
30°	10.8	9.8	–0.7	12.3
15°	7.0	5.3	–1.2	9.4
7.5°	3.9	2.8	–0.8	5.4
5°	2.6	1.9	–0.6	3.7
3.75°	2.0	1.4	–0.4	2.8
1°	0.6	0.4	–0.1	0.78
0.5°	0.3	0.2	–0.06	0.4

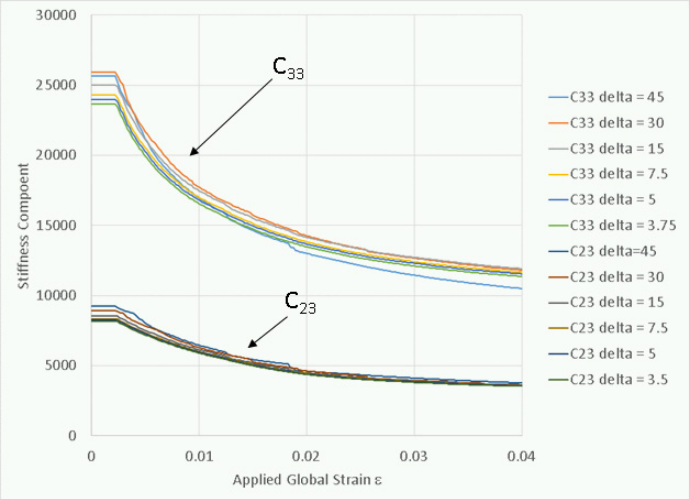

Figure 30.—Evolution of nonlinear stiffness components C_{33} and C_{23} calculated using Equations (6) and (7) for a range of orientation angle increments $\Delta\theta$, $\Delta\phi$ (delta).

9.4 Error and Uncertainty in Structural Sizing

Structural sizing is a method used to arrive at rapid and robust preliminary and/or intermediate designs, but does not contain all the details that exist in the real structure. Although a concerted endeavor was executed to alleviate some of the uncertainties resulting from error introduces at various stages in the multiscale modeling, many uncertainties within the sizing model still persist. For instance, only two load cases were considered and furthermore these are approximations of the loads the structure will actually endure. It is possible that the actual in-service loads are more severe. In addition, the failure criteria employed are mostly empirical, and while they attempt to reflect reality, they do not capture the true underlying physics of the damage and failure mechanisms that may arise. Finally, many structural details are omitted from the model including cut-outs, detailed representation of the joints, and the adjacent structures in SLS stack. It is incredibly difficult to quantify these uncertainties without detailed testing and analysis. As such, it is common practice to add a 25 percent mass penalty to preliminary designs in addition to the standard factors of safety.

9.5 Other Sources of Error and Uncertainty: Fiber Misalignment

For the OHC simulations presented in Section 8.2.5 it was assumed that a uniform fiber misalignment angle of 1° was present in all the plies. In reality, this misalignment may be more sever and nonuniform especially in curved sections, near cut-outs, and ply build-ups/drop-offs. To investigate the sensitivity of OHC to fiber misalignment OHC FEM simulations of a unidirectional specimen were conducted with 1° and 3° initial, uniform fiber misalignment. The simulations predicted that a 3° initial misalignment resulted in only ~8 percent reduction in the OHC strength of the unidirectional composite.

Conclusions

The ICME project was successful in designing a new material system for the NASA SLS CEUS forward skirt structure in meeting the designated metrics for success. Specifically:

- A suite of multiscale modeling tools was used to efficiently and accurately drive the design of a new composite material that was optimized for mechanical integrity of the skirt structure. The design-driven approach was complimented with limited experiments to further facilitate the optimization process. The whole effort was performed in a fraction of the time that would have been required for the Edisonian approach, and at a fraction of the cost.
- The simulations indicate that a significant enhancement of the OHC strength of the composite system is possible through the addition of GNP to the matrix. This improved OHC strength was translated into improved stress allowables, which were used in the design of the compression-dominated skirt structure. The structure, designed using aluminum honeycomb sandwich panels with facesheets composed of the AS4/EPON862 carbon fiber composite, both with and without GNP enhancements added to the matrix, demonstrated a significant payoff from the improved properties offered by the addition of GNP. The GNP enhanced structure showed a 22 percent reduction in mass, while both designs are equal in terms of ease of manufacture.
- The reduced mass results in a 45 percent cost reduction in manufacturing (Section 3.0).
- A multiscale modeling workflow encompassing 6 disparate length scale was successfully developed. Structural performance (i.e., weight savings) is linked to processing parameters (GNP volume fraction and GNP dispersion) and manufacturability in an optimized and iterative fashion.
- The combination of experimental testing and multiscale modeling and simulation provided four Michigan Tech PhD students valuable research experience and significant data that will contribute towards the completion of their PhD work.

Moreover, all key aspects of ICME were employed to complete this project including multiscale modeling, experimental characterization and visualization, data management, visualization, error and uncertainty quantification, and education.

Of course, the major improvements in properties and performance cited above would need to be validated through rigorous OHC testing of the material, which was beyond the scope of the present investigation. This demonstration only considered one configuration for the GNP enhanced system. Future work can investigate including other volume fractions of CF and GNP, and GNP dispersion levels, in order to expand the design space, including functionally graded GNP throughout the system. Further, a different carbon fiber and matrix system could improve the properties and performance further. However, as a combined experimental and analysis ICME study, spanning 9 orders of magnitude in length scale, the results presented herein indicate a dramatic level of success, as well as the power and potential of ICME and multiscale modeling for composite materials.

References

1. Sleight, D.W., Kosareo, D.N., and Thoma, S.D., *Composite Interstage Structural Concept Down Select Process and Results, in SAMPE Conference*. 2012: Baltimore, MD.
2. Mann, T., Smeltzer, S., Grenoble, R., Mason, B., Rosario, S., and Fairbairn, B., *Sizing and Lifecycle Cost Analysis of an Ares V Composite Interstage, in 53rd AIAA/ASME/ASCE/AHS/ASC Structures, Structural Dynamics, and Materials Conference*. 2012: Honolulu, HI.
3. Hadden, C.M., Klimek-McDonald, D.R., Pineda, E.J., King, J.A., Reichanadter, A.M., Miskioglu, I., Gowtham, S., and Odegard, G.M., "Mechanical properties of graphene nanoplatelet/carbon fiber/epoxy hybrid composites: Multiscale modeling and experiments." Carbon, vol. 95, 2015, pp. 100–112.
4. Budiansky, B. and Fleck, N.A., "Compressive Failure of Fiber Composites." *Journal of the Mechanics and Physics of Solids*, vol. 41, 1, 1993, pp. 183–211.
5. Kumar, A., Li, S.B., Roy, S., King, J.A., and Odegard, G.M., "Fracture properties of nanographene reinforced EPON 862 thermoset polymer system." *Composites Science and Technology*, vol. 114, 2015, pp. 87–93.
6. Fikes, J.C., Jackson, J.R., Richardson, S.W., Thomas, A.D., Mann, T.O., and Miller, S.G., *Composites for Exploration Upper Stage, NASA/TM—2016-219433*. 2016.
7. https://www.nasa.gov/exploration/systems/sls/multimedia/sls-block1B-mission-concepts.html.
8. Ballard, C., *Personal Communication, Senior Planner, Zyvex Performance Materials*. 2017.
9. Denton, G., *Plascore Quotation, Plascore Customer Service Representative, Plascore, Zeeland, MI*. 2017.
10. http://www.grantadesign.com/products/mi/index.htm.
11. Allen, M.P. and Tildesley, D.J., *Computer Simulation of Liquids*. Oxford University Press, Oxford, 1987.
12. http://lammps.sandia.gov/.
13. Paley, M. and Aboudi, J., "Micromechanical Analysis of Composites by the Generalized Cells Model." Mechanics of Materials, vol. 14, 2, 1992, pp. 127–139.
14. Aboudi, J., Arnold, S.M., and Bednarcyk, B.A., *Micromechanics of Composite Materials*: A Generalized Multiscale Analysis Approach. Elsevier, Inc., New York, 2013.
15. Bednarcyk, B.A., Aboudi, J., and Arnold, S.M., "The effect of general statistical fiber misalignment on predicted damage initiation in composites." Composites Part B-Engineering, vol. 66, 2014, pp. 97–108.
16. Bednarcyk, B.A. and Arnold, S.M., *MAC/GMC user's manual - keywords manual. NASA/TM—2002-212077/vol 2*. 2002.
17. Bednarcyk, B.A., Aboudi, J., and Arnold, S.M., "Micromechanics Modeling of Composites Subjected to Multiaxial Progressive Damage in the Constituents." AIAA Journal, vol. 48, 7, 2010, pp. 1367–1378.

18. Nemeth, N.N., Bednarcyk, B.A., Pineda, E.J., Walton, O.J., and Arnold, S.M., *Stockastic-Strength-Based Damage Simulation Tool for Ceramic Matrix and Polymer Matrix Composite Structures*. *NASA/TM—2016-219113*. 2016.
19. Christensen, R.M. and Waals, F.M., "Effective Stiffness of Randomly Oriented Fiber Composites." Journal of Composite Materials, vol. 6, 1972, pp. 518–535.
20. *ASTM D6484-2004. Standard Test Method for Open-Hole Compressive Strength of Polymer Matrix Composite Laminates*.
21. Schapery, R.A., "*Prediction of Compressive Strength and Kink Bands in Composites Using a Work Potential*." International Journal of Solids and Structures, vol. 32, 6–7, 1995, pp. 739–765.
22. Basu, S., Waas, A.M., and Ambur, D.R., "A Macroscopic Model for Kink Banding Instabilities in Fiber Composites." *Journal of Mechanics of Materials and Structures*, vol. 1, 6, 2006, pp. 979–1000.
23. Schapery, R.A., "A Theory of Mechanical-Behavior of Elastic Media with Growing Damage and Other Changes in Structure." *Journal of the Mechanics and Physics of Solids*, vol. 38, 2, 1990, pp. 215–253.
24. Schapery, R.A. and Sicking, D.L., *A Theory of Mechanical Behavior of Elastic Media with Growing Damage and Other Changes in Structure, in Mechanical Behavior of Materials*, A. Bakker, Editor. 1995, Delft University Press: Netherlands. pp. 45–76.
25. Sicking, D.L., *Mechanical Characterization of Nonlinear Laminated Composites with Transverse Crack Growth*. 1992, Texas A&M University: College Station, TX.
26. Pineda, E.J. and Waas, A.M., "Numerical implementation of a multiple-ISV thermodynamically-based work potential theory for modeling progressive damage and failure in fiber-reinforced laminates." *International Journal of Fracture*, vol. 182, 1, 2013, pp. 93–122.
27. Basu, S., Waas, A.M., and Ambur, D.R., "Prediction of progressive failure in multidirectional composite laminated panels." *International Journal of Solids and Structures*, vol. 44, 9, 2007, pp. 2648–2676.
28. Pineda, E.J., Waas, A.M., Bednarcyk, B.A., Collier, C.S., and Yarrington, P.W., "Progressive damage and failure modeling in notched laminated fiber reinforced composites." International Journal of Fracture, vol. 158, 2, 2009, pp. 125–143.
29. Craft, W.J. and Christensen, R.M., "Coefficient of Thermal-Expansion for Composites with Randomly Oriented Fibers." *Journal of Composite Materials*, vol. 15, Jan, 1981, pp. 2–20.
30. Klimek-McDonald, D.R., *Mechanical Properties of Graphene Nanoplatele/Epoxy Composites*, *PhD dissertation*. 2015, Michigan Technological University.
31. Littell, J.D., Ruggeri, C.R., Goldberg, R.K., Roberts, G.D., Arnold, W.A., and Binienda, W.K., "Measurement of epoxy resin tension, compression, and shear stress-strain curves over a wide range of strain rates using small test specimens." *Journal of Aerospace Engineering*, vol. 21, 3, 2008, pp. 162–173.
32. Bandyopadhyay, A., Valavala, P.K., Clancy, T.C., Wise, K.E., and Odegard, G.M., "Molecular modeling of crosslinked epoxy polymers: The effect of crosslink density on thermomechanical properties." *Polymer*, vol. 52, 11, 2011, pp. 2445–2452.
33. Klimek-McDonald, D.R., King, J.A., Miskioglu, I., Pineda, E.J., and Odegard, G.M., "Determination and Modeling of Mechanical Properties for Graphene Nanoplatelet/Epoxy Composites." *Polymer Composites, Accepted for publication*, vol., 2017.
34. https://hypersizer.com/.
35. http://www.mscsoftware.com/product/msc-nastran.
36. *xGnP Brand Graphene Nanoplatelets Product Information*. 2010: 3101 Grand Oak Drive, Lansing, MI.
37. Hexcel, *HexTow Continuous Carbon Fiber Product Literature*. 2011: Stamford, CT.
38. King, J.A., Klimek, D.R., Miskioglu, I., and Odegard, G.M., "Mechanical properties of graphene nanoplatelet/epoxy composites." *Journal of Composite Materials*, vol. 49, 6, 2015, pp. 659–668.

39. MIL-HDBK-17-2E, *Department of Defense Handbook: Composite Materials Handbook, Volume 2 - Polymer Matrix Composites Materials Properties*, January 23, 1997.
40. Engelstad, S.P. and Clay, S.B., "Comparison of composite damage growth tools for static behavior of notched composite laminates." *Journal of Composite Materials*, vol. 51, 10, 2017, pp. 1493–1524.
41. http://www.hexcel.com/user_area/content_media/raw/CR3_us.pdf.